Graphical Abstract

Growth of shell-like soft biological tissues under mechanical loading

Farzam Dadgar-Rad,Amirhossein N. Dorostkar,Mokarram Hossain

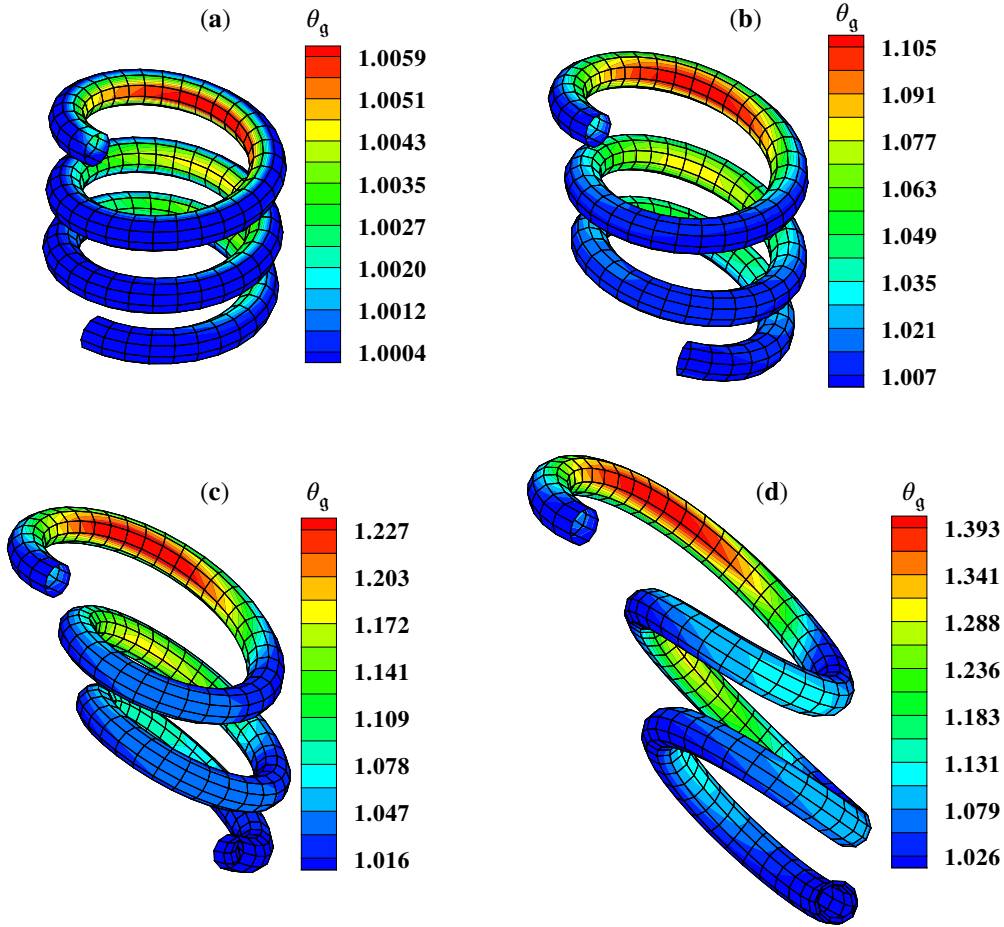

Figure **GA**: Growth of a helix under self-weight, (**a**): deformed shape and contour plot of the growth multiplier $\theta_\mathfrak{g}$ at the end of loading ($t = 1$ s), (**b**): grown stage at $t = 11$ s, (**c**): grown stage at $t = 21$ s, (**d**): grown stage at $t = 31$ s

In this example, the growth mechanics of a helix under its weight is investigated. The cross-section of the helix is a circle of radius $a = 5$ mm and the thickness $h = 1$ mm. The average radius of the helix is $b = 25$ mm. The angle $\zeta^1 \in [0, 2\pi]$ describes the circumference of the cross-section. Moreover, the angle $\zeta^2 \in [0, \zeta^2_{\max}]$ is used to describe the centreline of the helix. In this work, $\zeta^2_{\max} = 6\pi$ is employed, which creates a helix with three complete loops. The equation of the referential centreline is given by $X_1^\mathfrak{c} = b\cos\zeta^2$, $X_2^\mathfrak{c} = b\sin\zeta^2$, and $X_3^\mathfrak{c} = \frac{p}{2\pi}\zeta^2$. Here, p is the pitch of the helix and is considered to be 12.5 mm. The material parameters are considered to be $\mu = 0.0385$ MPa, $\nu = 0.48$, $\theta_\mathfrak{g}^{\max} = 2.4$, $\gamma = 2$, $T = 0.1$ s, and $\theta_\mathrm{e}^{\mathrm{crit}} = 1$, and $\rho_0 = 20$ kg/m^3. The top cross-section of the helix, at $\zeta^2 = \zeta^2_{\max}$, is assumed to be fixed. In the first step, the weight of the helix is applied gradually in $t_{\mathfrak{l}} = 1$ s. The growth process under the maximum weight is then simulated in $t_\mathfrak{g} = 30$ s. The deformed shapes of the helix at four stages, namely at $t \in \{1, 11, 21, 31\}$ (s) are illustrated in Figure **GA** (**a**–**d**). The contour plots of the growth parameter $\theta_\mathfrak{g}$ are also displayed on the deformed shapes. The maximum value of $\theta_\mathfrak{g}$ is obtained to be 1.45.

Highlights

Growth of shell-like soft biological tissues under mechanical loading

Farzam Dadgar-Rad,Amirhossein N. Dorostkar,Mokarram Hossain

- A shell formulation for finite growth of thin biological tissues is developed.

- The model is based upon a seven-parameter shell model and strain-driven growth mechanics.

- A nonlinear FE formulation in the material framework for the numerical solution of the problems is developed.

- Benchmark examples demonstrating the accuracy and capability of the proposed formulation are provided.

Growth of shell-like soft biological tissues under mechanical loading

Farzam Dadgar-Rad[a], Amirhossein N. Dorostkar[a] and Mokarram Hossain[b,*]

[a]*Faculty of Mechanical Engineering, University of Guilan, Rasht, 695013, Guilan, Iran*
[b]*Zienkiewicz Institute for Modelling, Data and AI, Faculty of Science and Engineering, Swansea University, SA1 8EN, UK*

ARTICLE INFO

Keywords:
Growth mechanics
Soft tissue
Shell
Large deformation
Finite Element Method

ABSTRACT

Application of mechanical loading to soft biological tissues plays a central role in tissue engineering. Mechanical stimuli convert into intracellular biochemical activity, referred to as mechanotransduction, and lead to the growth of tissues. In most practical applications, the mechanotransduction phenomenon has been examined on thin tissues in two- or three-dimensional space. Accordingly, a phenomenological finite growth formulation for shell-like soft tissues under mechanical loading is presented in this work. The basic kinematic and kinetic quantities besides the constitutive response are formulated. The unconditionally stable implicit Euler-backward scheme is employed to solve the evolution equation of the growth parameter. Moreover, a nonlinear finite element formulation is developed, which can provide numerical solutions under arbitrary geometry, loading, and boundary conditions. Several examples are presented that demonstrate the applicability and performance of the formulation. The results indicate that finite growth as well as finite deformation of thin tissues under mechanical input can be successfully predicted by the present formulation.

1. Introduction

Traditional engineering materials undergo infinitesimal or finite deformations under mechanical loading. However, biomaterials can exhibit some additional behaviors including growth, remodeling, morphogenesis, change of mass, and adaptation, besides deformation, in response to mechanical stimuli [1, 2]. Moreover, applying mechanical loading, e.g., stretching, is a technique for improving the strength, functionality, and growth of a wide variety of organs in tissue engineering [3–6]. Accordingly, developing reliable theoretical and numerical tools play a crucial role in predicting the morphological patterns and behavior of these materials in various applications such as tissue engineering and reconstructive surgeries [7–9].

A wide variety of formulations for the mathematical modeling of the growth and remodeling processes have been developed in the literature, e.g., Refs. [2, 10–16]. A modern treatment of the growth phenomenon based on the notion of an evolving Riemannian material manifold, constructed via a time-dependent material metric, was formulated by Yavari [17]. Moreover, formulations of growth and remodeling based on the couple stress and micromorphic continuum theories have been also developed by Javadi et al. [18, 19].

The continuum formulations of growth mechanics often start from the multiplicative decomposition of the deformation gradient into the growth and elastic parts, e.g., [10, 20–25]. The growth part of the deformation gradient is

*Corresponding author

f.dadgar@guilan.ac.ir (F. Dadgar-Rad); ahnd16@yahoo.com (A.N. Dorostkar); mokarram.hossain@swansea.ac.uk (M. Hossain)
ORCID(s): 0000-0003-1546-2446 (F. Dadgar-Rad); 0009-0000-1603-7260 (A.N. Dorostkar); 0000-0002-4616-1104 (M. Hossain)

often called the growth function or growth field. The problems dealing with the growth of soft tissues may be divided into three categories. In the first category, the growth function is specified, or its corresponding function can be easily integrated, and the final deformed shape of the body is to be determined, e.g., Refs. [26–31]. In the second category, which is used for shape-programming purposes, the objective is to find an unknown growth field such that a target stress-free current configuration can be achieved, e.g., Refs. [32–37]. In the third category, which is the subject of the present study, both the growth field and the deformed shape are unknown (e.g., Refs. [38–47]). More precisely, a soft tissue is subjected to specified mechanical loading and boundary conditions. Both *mechanical equilibrium* equation and the *evolution equation* of growth must be solved by analytical or numerical methods. After solving these equations, the growth function and the final deformed shape of the growing body are obtained. Clearly, this category of problems plays a central role in the controllable growth of organs and the improvement of their mechanical properties in tissue engineering (e.g., [4, 6]).

On the other hand, *thin* growing organs such as skin, leaves, and wings of insects are widely observed in nature. Accordingly, there have been published several research papers that model these organs as plates [33–35, 48–51], and shells [27, 36, 52, 54, 57]. In particular, the formulation proposed by Rausch and Kuhl [52] is based on adding the growth effects to the Kirchhoff–Love shell model in the commercial software ABAQUS. It is noted that for a standard FE formulation of Kirchhoff–Love shell model, C^1-continuous interpolation functions are needed. However, ABAQUS employs C^0 shape functions through a mixed displacement-rotation discretization [53]. The model developed by Zheng et al. [54] for the growth analysis of thin soft tissues is based on *solid-shell* element. It is noted that in this type of shell element, the nodal degrees of freedom are defined on the top and bottom surfaces of a hexagonal element. Accordingly, the main strategy is similar to 3D solid elements. Only the displacement field of shell-type structures is enforced on the geometry of the hexagonal element. Moreover, the number of unknown nodal variables is more than classical shell elements that define the nodal unknowns on the midsurafce of the shell.

It is noted that modern geometric and numerical techniques, e.g., isogeometric analysis [55], have been used to model the deformation of biological tissues. In particular, Dortdivanlioglu et al. [24] simulated the morphological instabilities of a thin growing film on a compliant substrate using isogeometric analysis. In another study, Tepole et al. [56] developed an isogeometric-based finite element formulation for the numerical simulation of biological membranes based on the Kirchhoff–Love shell model. It is noted that the growth effect has not been included in their formulation. From a completely different point of view, the formulation elaborated by Sadik et al. [57] is the extension of the geometric theory of growth developed previously in [17] to thin organs. To the authors' knowledge, numerical computations based on the mentioned geometric formulation have not been yet presented in the literature.

From the review of the literature, it is found that a few research works have been conducted on developing general and computationally robust formulations for the growth analysis of shell-like soft tissues. Accordingly, the purpose of

this work is to develop a novel formulation by combining the original 7-parameter shell model proposed by Sansour (e.g., [58, 59]) with the strain-driven growth mechanics (e.g., [39–44]). From the computational point of view, the corresponding finite element formulation of the developed shell model is also presented. Compared with the previously notable developed formulations (e.g., [52, 54]), the main features of the present contribution are as follows:

- Rather than using Kirchhoff–Love shell model [52], or solid-shell element with nodal variables at the corners of a hexahedral [54], a new formulation based on Sansour's 7-parameter shell model [58, 59] is elaborated. The present formulation falls in the category of *geometrically exact Mindlin–Reissner shell models* in computational mechanics terminology. The nodal degrees of freedom are defined on the midsurface of the shell and the resulting formulation is C^0-continuous. It is noted that in contrast to higher-order elements, C^0 elements lead to smaller bandwidth of the global stiffness matrix.

- One of the main advantages of the present shell model is that three-dimensional constitutive equations can be directly employed in the calculation of stress and element stiffness matrix. This circumvents modifying the constitutive equations to satisfy the plane stress assumption in traditional shell formulations. It is noted that satisfaction of the plane stress assumption is not easy for arbitrary constitutive equations.

- The enhanced assumed strain (EAS) method [60–63] is employed to alleviate the well-known locking phenomenon in numerical computations.

In the rest of this research, the kinematics of the shell model is presented in Section 2. The basics of the mechanical growth theory, evolution equation, and its solution procedure are provided in Section 3. Section 4 deals with the variational formulation of the problem, where an EAS formulation based on the Hu–Washizu principle and including the growth effects is constructed. A Total Lagrangian FE formulation is developed in Section 5. Section 6 demonstrates the effectiveness of the proposed formulation through several examples. Finally, a summary of the work is given in Section 7.

Notation: Throughout, Greek indices (subscripts or superscripts) range over $\{1, 2\}$, Latin indices have the range $\{1, 2, 3\}$, and the usual summation convection is applied. Upper-case indices with calligraphic font, e.g., $\mathcal{I}$, take the values specified in the corresponding equations. For the two arbitrary 2nd-order tensors $\mathbf{X}$ and $\mathbf{Y}$, three different 4th-order tensors $(\mathbf{X} \otimes \mathbf{Y})_{ijkl} = X_{ij}Y_{kl}$, $(\mathbf{X} \boxtimes \mathbf{Y})_{ijkl} = X_{il}Y_{kj}$, $(\mathbf{X} \bar{\boxtimes} \mathbf{Y})_{ijkl} = X_{il}Y_{jk}$, and $(\mathbf{X} \odot \mathbf{Y})_{ijkl} = X_{ik}Y_{jl}$ are defined in this work.

2. Kinematics of the shell model

The geometry of a deforming shell in the reference and current configurations is illustrated in Fig. 1. The reference and current midsurfaces are denoted by S_0 and S, respectively. To quantize the kinematic tensors of the shell, a
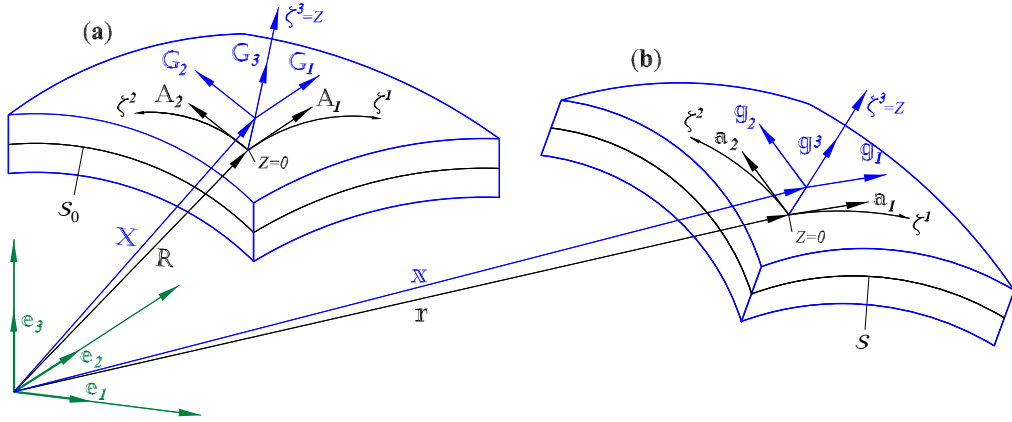
Figure 1: Geometry of a growing shell in the reference (**a**) and current (**b**) configurations (the vectors in the set $\{\mathbb{R}, \mathbb{A}_1, \mathbb{A}_2, \mathbb{r}, \mathbb{a}_1, \mathbb{a}_2\}$ belong the undeformed and deformed midsurfaces with $Z = 0$. The other quantities, namely $\{\mathbb{X}, \mathbb{G}_1, \mathbb{G}_2, \mathbb{G}_3, \mathbb{x}, \mathbb{g}_1, \mathbb{g}_2, \mathbb{g}_3\}$ are defined at the elevation $Z \neq 0$ with respect to the midsurfaces)

reference Cartesian coordinate with the basis vectors $\{\mathbb{e}_1, \mathbb{e}_2, \mathbb{e}_3\}$ at an arbitrary origin is constructed. Additionally, the convective coordinate system $\{\zeta^1, \zeta^2, \zeta^3\}$ at each material point of S_0 is considered, so that ζ^α and ζ^3 are, respectively, tangent and perpendicular to it. For simplicity, the notation Z is used instead of ζ^3 in the rest of this paper.

As usual in the shell formulations, the position vector of the material points in the reference configuration is given by

$$\mathbb{X}(\zeta^1, \zeta^2, z) = \mathbb{R}(\zeta^1, \zeta^2) + Z\mathbb{D}(\zeta^1, \zeta^2), \tag{1}$$

where $\mathbb{D}$ and $\mathbb{R}$ are the outward unit normal and the position vector on the reference midsurface, respectively. In this work, the 7-parameter shell model proposed by Sansour (e.g., [58, 59]) is extended to include the growth effects. The midsurface displacement $\mathbb{u}$ takes $\mathbb{R}$ to the new position $\mathbb{r}$ on the deformed midsurface, namely $\mathbb{r} = \mathbb{R} + \mathbb{u}$. Moreover, the director displacement $\mathbb{w}$ takes $\mathbb{D}$ to the current director $\mathbb{v}$ via the relation $\mathbb{a}_3 = \mathbb{D} + \mathbb{w}$. Additionally, the scalar field ψ is introduced as a measure of the through the thickness stretching. Accordingly, the position of the material particles in the current configuration obeys the following relation [58, 59]:

$$\mathbb{x} = \boldsymbol{\phi}(\mathbb{X}, t) = \mathbb{r}(\zeta^1, \zeta^2, t) + [Z + Z^2\psi(\zeta^1, \zeta^2, t)]\mathbb{a}_3(\zeta^1, \zeta^2, t), \tag{2}$$

where $\boldsymbol{\phi}$ is the deformation mapping and $t \geq 0$ is the time. From Eqs. (1) and (2), the reference covariant basis vectors $\mathbb{G}_i = \frac{\partial \mathbb{X}}{\partial \zeta^i}$, and the current ones $\mathrm{g}_i = \frac{\partial \mathrm{x}}{\partial \zeta^i}$, are calculated to be

$$
\left.\begin{aligned}
\mathbb{G}_\alpha &= \mathbb{A}_\alpha + Z\mathbb{D}_{,\alpha}, \quad \mathbb{G}_3 = \mathbb{A}_3 = \mathbb{D} \\
\mathrm{g}_\alpha &= \mathrm{a}_\alpha + Z\mathrm{a}_{3,\alpha} + Z^2(\psi\mathrm{a}_3)_{,\alpha}, \quad \mathrm{g}_3 = (1 + 2Z\psi)\mathrm{a}_3
\end{aligned}\right\},
\tag{3}
$$

where $\{\bullet\}_{,\alpha}$ denotes $\frac{\partial}{\partial \zeta^\alpha}\{\bullet\}$. Additionally, $\mathbb{A}_\alpha = \mathbb{R}_{,\alpha}$ and $\mathrm{a}_\alpha = \mathrm{r}_{,\alpha} = \mathbb{A}_\alpha + \mathrm{u}_{,\alpha}$ are the covariant basis vectors tangent to S_0 and S, respectively. Furthermore, the relation $\mathrm{a}_3 = \mathrm{g}_{3|Z=0}$ holds. The covariant components of the reference metric tensor at $Z \in [-h/2, h/2]$ are calculated via the relation $G_{ij} = \mathbb{G}_i \cdot \mathbb{G}_j$, and the contravariant components of the reference metric follow the property $G^{ik}G_{kj} = \delta^i_j$. Additionally, the reference contravariant basis vectors are given by $\mathbb{G}^i = G^{ij}\mathbb{G}_j$. At the reference midsurface, with $Z = 0$, the quantities in the set $\{G_{ij}, G^{ij}, \mathbb{G}_i, \mathbb{G}^i\}$ are, respectively, replaced by $\{A_{ij}, A^{ij}, \mathbb{A}_i, \mathbb{A}^i\}$. Furthermore, similar relations hold in the current configuration. It is noted that the relation $\mathbb{D}_{,\alpha} = -\mathbf{K}\mathbb{A}_{,\alpha}$ holds (e.g., Ref. [64]), where $\mathbf{K}$ is the curvature tensor on S_0. With the aid of Eqs. (2) and (3) the deformation gradient is approximated as follows:

$$
\mathbf{F} = \mathrm{g}_i \otimes \mathbb{G}^i \approx \mathbf{F}^{[0]} + Z\mathbf{F}^{[1]} \quad \text{with} \quad \mathbf{F}^{[0]} = \mathrm{a}_i \otimes \mathbb{G}^i, \quad \mathbf{F}^{[1]} = \mathrm{a}_{3,\alpha} \otimes \mathbb{G}^\alpha + 2\psi\mathrm{a}_3 \otimes \mathbb{D}.
\tag{4}
$$

Moreover, the term involving Z^2 in g_α has been neglected. From Eq. (4) the compatible right Cauchy–Green deformation tensor $\mathbf{C}$ may be written as

$$
\mathbf{C} = \mathbf{F}^\mathsf{T}\mathbf{F} \approx \mathbf{C}^{[0]} + Z\mathbf{C}^{[1]},
\tag{5}
$$

where $\mathbf{C}^{[0]} = \mathbf{F}^{[0]\mathsf{T}}\mathbf{F}^{[0]} = C^{[0]}_{ij}\mathbb{G}^i \otimes \mathbb{G}^j$ and $\mathbf{C}^{[1]} = \mathbf{F}^{[0]\mathsf{T}}\mathbf{F}^{[1]} + \mathbf{F}^{[1]\mathsf{T}}\mathbf{F}^{[0]} = C^{[1]}_{ij}\mathbb{G}^i \otimes \mathbb{G}^j$ are two symmetric second-order tensors. Based on Eqs. (4) and (5), the components of $\mathbf{C}^{[\mathcal{I}]}$ ($\mathcal{I} = 0, 1$) may be written as

$$
\left.\begin{aligned}
C^{[0]}_{ij} &= \mathrm{a}_i \cdot \mathrm{a}_j, \quad C^{[1]}_{\alpha\beta} = \mathrm{a}_\alpha \cdot \mathrm{a}_{3,\beta} + \mathrm{a}_\beta \cdot \mathrm{a}_{3,\alpha} \\
C^{[1]}_{\alpha 3} &= \mathrm{a}_3 \cdot (\mathrm{a}_{3,\alpha} + 2\psi\mathrm{a}_\alpha), \quad C^{[1]}_{33} = 4\psi\mathrm{a}_3 \cdot \mathrm{a}_3
\end{aligned}\right\}.
\tag{6}
$$

3. Mechanical growth and evolution equation

In this section, the kinematics and evolution equation of finite growth are presented. For more details, Refs. [1, 10–12] are suggested. To describe the kinematics of growth, the deformation gradient $\mathbf{F}$ is decomposed multiplicatively

as (e.g., [10, 12, 21])

$$\mathbf{F} = \mathbf{F}_e \mathbf{F}_g, \quad J_e = \det \mathbf{F}_e, \quad J_g = \det \mathbf{F}_g, \quad J = \det \mathbf{F} = J_e J_g, \tag{7}$$

where $\mathbf{F}_g$ and $\mathbf{F}_e$ are, respectively, the growth and elastic parts of the deformation gradient tensor. Clearly, the local growth deformation gradient $\mathbf{F}_g$ maps the infinitesimal material line elements from the reference configuration $\mathcal{B}_0$ to the intermediate configuration $\bar{\mathcal{B}}$. The growth and elastic form of the right Cauchy–Green deformation tensor is defined by

$$\mathbf{C}_e = \mathbf{F}_e^\top \mathbf{F}_e = \mathbf{F}_g^{-\top} \mathbf{C} \mathbf{F}_g^{-1}, \quad \mathbf{C}_g = \mathbf{F}_g^\top \mathbf{F}_g. \tag{8}$$

Obviously, $\mathbf{C}_e$ is the push-forward of $\mathbf{C}$ to the intermediate configuration by $\mathbf{F}_g$. It is easy to prove that for any general invertible second-order tensor $\mathbf{T}$ the following relations hold:

$$\frac{\partial \mathbf{T}^{-1}}{\partial \mathbf{T}} = -\mathbf{T}^{-1} \odot \mathbf{T}^{-1}, \quad \frac{\partial \mathbf{T}^{-\top}}{\partial \mathbf{T}} = -\mathbf{T}^{-\top} \boxtimes \mathbf{T}^{-\top}. \tag{9}$$

From Eqs. (8) and (9) it follows that the partial derivatives of $\mathbf{C}_e$ with respect to $\mathbf{C}$ and $\mathbf{F}_g$ are given by

$$\left. \begin{aligned} \left. \frac{\partial \mathbf{C}_e}{\partial \mathbf{C}} \right|_{\mathbf{F}_g} &= \frac{1}{2} (\mathbf{F}_g^{-\top} \odot \mathbf{F}_g^{-1} + \mathbf{F}_g^{-\top} \boxtimes \mathbf{F}_g^{-1}) \\ \left. \frac{\partial \mathbf{C}_e}{\partial \mathbf{F}_g} \right|_{\mathbf{F}} &= -(\mathbf{F}_g^{-\top} \boxtimes \mathbf{C}_e + \mathbf{C}_e \odot \mathbf{F}_g^{-1}) \end{aligned} \right\}, \tag{10}$$

which will be used in the next developments.

Depending on the nature of growth in a living body, it is possible to consider different forms for the growth deformation gradient $\mathbf{F}_g$. For example, for the case of *isotropic growth* in all directions, the relation $\mathbf{F}_g = \theta_g^{1/3} \mathbf{I}$ is considered, where the parameter θ_g is referred to as the *growth multiplier*. For the present shell model, it is assumed that growth does not occur in the thickness direction. In other words, it is assumed that the growth phenomenon takes place isotropically in the plane perpendicular to the normal vector $\mathbb{D}$, and is referred to as the *transversely isotropic growth*. The basic idea is that the change in the growth of an organ remains almost constant under the action of the growth part of the deformation gradient $\mathbf{F}_g$. However, it is important to notice that the organ thickness changes under the action of the elastic part of the deformation gradient $\mathbf{F}_e$. This assumption has been frequently used in the literature in the growth modeling of thin tissues such as skin (e.g., [39–44, 52]). Accordingly, the expression for $\mathbf{F}_g$ may be
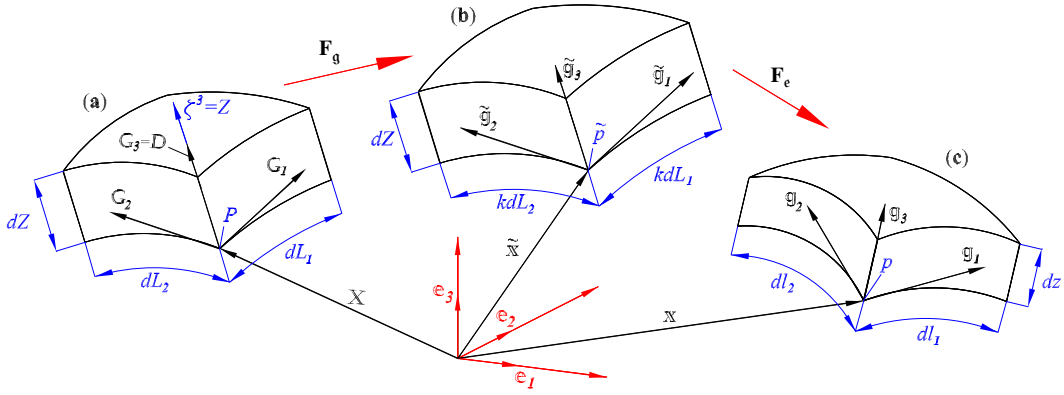
Figure 2: Deformation of an infinitesimal growing shell element under the action of the multiplicative decomposition $\mathbf{F} = \mathbf{F}_e\mathbf{F}_g$ (with $\mathbf{F}_g = k(\mathbf{I} - \mathbb{D} \otimes \mathbb{D}) + \mathbb{D} \otimes \mathbb{D}$ and $k = \sqrt{\theta_g}$): reference (**a**), intermediate (**b**), and current (**c**) configurations.

written as (e.g., Refs. [39, 52])

$$\mathbf{F}_g = \sqrt{\theta_g}(\mathbf{I} - \mathbb{D} \otimes \mathbb{D}) + \mathbb{D} \otimes \mathbb{D}. \tag{11}$$

The geometry of deformation under the multiplicative decomposition $\mathbf{F} = \mathbf{F}_e\mathbf{F}_g$ is illustrated in Fig. 2. An infinitesimal volume element of dimensions $dL_1 \times dL_2 \times dZ$ at the point P and the elevation Z with respect to the referential midsurface $\mathcal{S}_0$ is depicted in Fig. 2(**a**). In the growth stage, under the action of $\mathbf{F}_g$ as expressed in Eq. (11), the dimensions of the element in the intermediate configuration will be $(kdL_1) \times (kdL_2) \times dZ$, with $k = \sqrt{\theta_g}$. In other words, as can be seen in Fig. 2(**b**), the thickness of the element remains unchanged under the action of $\mathbf{F}_g$. This indicates that the effect of $\mathbf{F}_g$ manifests itself as the area change from $\mathrm{d}\mathcal{A}_0 = dL_1 dL_2$ to $\mathrm{d}\tilde{\mathcal{A}} = (kdL_1)(kdL_2) = k^2 dA_0 = \theta_g dA_0$. In particular, one may write $\mathbf{F}_g = \tilde{\mathbb{g}}_i \otimes \mathbb{G}^i$, where $\tilde{\mathbb{g}}_i$ are the covariant basis vectors at intermediate configuration. From this point and Eq. (11) it follows that

$$\tilde{\mathbb{g}}_\alpha = \sqrt{\theta_g}\mathbb{G}_\alpha, \quad \tilde{\mathbb{g}}_3 = \mathbb{G}_3 = \tilde{\mathbb{D}} = \mathbf{F}_g\mathbb{D} = \mathbb{D}, \quad J_g = \theta_g, \quad \mathbf{F}_g^{-\top}\mathbb{D} = \mathbb{D}. \tag{12}$$

The elastic deformation stage is displayed in Fig. 2(**c**), where thickness change, further in-plane stretch, and bending type motion are applied to the element under the action of $\mathbf{F}_e$.

Now let the pairs $(\mathrm{d}\mathcal{A}_0, \mathbb{D})$, $(\mathrm{d}\tilde{\mathcal{A}}, \tilde{\mathbb{D}})$, and $(\mathrm{d}\mathcal{A}, \mathbb{n})$ be the infinitesimal area elements and the corresponding outward unit normal vectors in the reference, intermediate, and current configurations, respectively. The well-known Nanson's formula between the pairs $(\mathcal{A}_0, \mathbb{D})$ and $(\mathcal{A}, \mathbb{n})$ is given by $\mathrm{d}\mathcal{A}\mathbb{n} = J\mathbf{F}^{-\top}\mathrm{d}\mathcal{A}_0\mathbb{D}$ (e.g., Ref. [65]). Similar relations hold between the different introduced pairs. In particular, employing Nanson's formula for the pairs $(\mathrm{d}\mathcal{A}_0, \mathbb{D})$ and $(\mathrm{d}\tilde{\mathcal{A}}, \tilde{\mathbb{D}})$,

and using Eqs. (11) and (12), it follows that

$$\frac{\mathrm{d}\tilde{\mathcal{A}}}{\mathrm{d}\mathcal{A}_0} = J_\mathfrak{g}|\mathbf{F}_\mathfrak{g}^{-\top}\mathbb{D}| = \theta_\mathfrak{g}, \tag{13}$$

indicating that the function $\theta_\mathfrak{g}$ measures the *area stretch* of an infinitesimal area element perpendicular to the normal vector $\mathbb{D}$ due to the growth of the body. Moreover, using Eq. (13) and employing Nanson's formula, the elastic and total area stretches, denoted respectively by θ and θ_e, may be written as

$$\left.\begin{aligned}\theta_e &= \frac{\mathrm{d}\mathcal{A}}{\mathrm{d}\tilde{\mathcal{A}}} = J_e|\mathbf{F}_e^{-\top}\tilde{\mathbb{D}}| = J_e\sqrt{\mathbf{C}_e^{-1}:(\tilde{\mathbb{D}}\otimes\tilde{\mathbb{D}})} \\ \theta &= \frac{\mathrm{d}\mathcal{A}}{\mathrm{d}\mathcal{A}_0} = \left(\frac{\mathrm{d}\mathcal{A}}{\mathrm{d}\tilde{\mathcal{A}}}\right)\left(\frac{\mathrm{d}\tilde{\mathcal{A}}}{\mathrm{d}\mathcal{A}_0}\right) = \theta_e\theta_\mathfrak{g} = J|\mathbf{F}^{-\top}\mathbb{D}| = J\sqrt{\mathbf{C}^{-1}:(\mathbb{D}\otimes\mathbb{D})}\end{aligned}\right\}. \tag{14}$$

The relation $\theta = \theta_e\theta_\mathfrak{g}$ indicates that the area stretch θ is multiplicatively decomposed into the elastic and growth parts.

The growth multiplier $\theta_\mathfrak{g}$ is the *internal variable* of the present formulation and can be determined by solving an *evolution equation*. It is noted that two types of formulations, namely *strain-driven* and *stress-driven* have been developed in the literature. The term strain-driven indicates that the evolution equation for θ depends upon the deformation gradient tensor (e.g., Ref. [39]). In contrast, in *stress-driven* growth formulations, the evolution equation depends on the stress tensor (e.g., Ref. [13]). In this work, the basic *strain-driven* growth formulation proposed in Ref. [39] is reformulated for the case of shell-like soft tissues. Accordingly, the evolution equation for θ is written as

$$\dot{\theta}_\mathfrak{g} = \hat{\beta}(\mathbf{F}_\mathfrak{g}, \mathbf{F}) = \beta(\theta_\mathfrak{g}, \theta) = \Phi_1(\theta_\mathfrak{g})\Phi_2(\theta_e) = \Phi_1(\theta_\mathfrak{g})\Phi_2\left(\frac{\theta}{\theta_\mathfrak{g}}\right), \tag{15}$$

where the scalar functions Φ_1 and Φ_2 are considered to be

$$\Phi_1 = \frac{1}{T}\left(\frac{\theta_\mathfrak{g}^{\max} - \theta_\mathfrak{g}}{\theta_\mathfrak{g}^{\max} - 1}\right)^\gamma, \quad \Phi_2 = \max\{0, \theta_e - \theta_e^{\mathrm{crit}}\} = \max\{0, \frac{\theta}{\theta_\mathfrak{g}} - \theta_e^{\mathrm{crit}}\}. \tag{16}$$

Here, T is referred to as the adaptation speed, γ is the growth exponent that affects the shape of the adaptation curve, and $\theta_\mathfrak{g}^{\max}$ is the maximum achievable value of the growth multiplier $\theta_\mathfrak{g}$. Moreover, θ_e^{crit} is the minimum required value of θ_e to activate the growth process in the tissue.

4. Variational formulation

In this section, the variational formulation of the problem by employing the enhanced assumed strain (EAS) method is developed. Following Refs. [13, 39, 43, 44], it is assumed that the elastic strain energy density is a function of the elastic right Cauchy–Green deformation tensor $\mathbf{C}_e$. More precisely, the function $\Psi = \Psi(\mathbf{C}_e)$ is considered to be the

elastic strain energy density per unit reference volume of the growing continuum body. In the next step, from Eq. (5) and motivated by the formulation of Sansour [58], the compatible Cauchy–Green deformation tensor $\mathbf{C}$ is enhanced in the following form:

$$\mathbf{C}^{\star} = \mathbf{C} + \tilde{\mathbf{C}}, \tag{17}$$

where $\tilde{\mathbf{C}}$ is referred to as the *enhancement tensor*. From Eqs. (8) and (17), the enhanced elastic Cauchy–Green deformation tensor, denoted by $\mathbf{C}_{\mathrm{e}}^{\star}$, is defined as

$$\mathbf{C}_{\mathrm{e}}^{\star} = \mathbf{F}_{\mathfrak{g}}^{-\top}\mathbf{C}^{\star}\mathbf{F}_{\mathfrak{g}}^{-1} = \mathbf{C}_{\mathrm{e}} + \tilde{\mathbf{C}}_{\mathrm{e}} \quad \text{with} \quad \tilde{\mathbf{C}}_{\mathrm{e}} = \mathbf{F}_{\mathfrak{g}}^{-\top}\tilde{\mathbf{C}}\mathbf{F}_{\mathfrak{g}}^{-1}. \tag{18}$$

The tensor $\tilde{\mathbf{C}}_{\mathrm{e}}$ may be regarded as the elastic enhancement tensor. The EAS method employs the three-field Hu–Washizu principle to obtain the weak form of the problem. In this work, independent variables are chosen to be the deformation field $\boldsymbol{\phi}$, the enhancement tensor $\tilde{\mathbf{C}}$, and the second Piola–Kirchhoff stress tensor $\mathbf{S}$. It is noted that the compatible right Cauchy–Green tensor $\mathbf{C}$ depends on $\boldsymbol{\phi}$ and is not an independent quantity. Accordingly, for a growing body, the following functional is introduced:

$$\Pi(\boldsymbol{\phi}, \tilde{\mathbf{C}}, \mathbf{S}) = \int_{\mathcal{V}_0} \left(\Psi(\mathbf{C}_{\mathrm{e}}^{\star}) - \frac{1}{2}\mathbf{S} : \tilde{\mathbf{C}} \right) \mathrm{d}\mathcal{V}_0 - \mathcal{W}^{\mathrm{ext}}. \tag{19}$$

It is worthwhile to note that the enhanced elastic Cauchy–Green tensor $\mathbf{C}_{\mathrm{e}}^{\star}$ is employed in the free energy density Ψ. Moreover, $\mathcal{W}^{\mathrm{ext}}$ as the work of external loads, given by

$$\mathcal{W}^{\mathrm{ext}} = \int_{\mathcal{V}_0} \mathbb{b}_0 \cdot \hat{\mathbb{u}}\,\mathrm{d}\mathcal{V}_0 + \int_{\partial\mathcal{V}_0} \mathbb{t}_0 \cdot \hat{\mathbb{u}}\,\mathrm{d}(\partial\mathcal{V}_0), \tag{20}$$

where $\mathbb{b}_0$ and $\mathbb{t}_0$ are the referential body force density and surface traction, respectively. Additionally, $\hat{\mathbb{u}} = \mathbb{x} - \mathbb{X}$ is the displacement field that can be calculated from Eqs. (1) and (2) in the present formulation. Furthermore, $\partial\mathcal{V}_0$ is the boundary surface of the undeformed shell. The functional Π is stationary if its first variation is zero, namely

$$\delta\Pi = \frac{1}{2}\int_{\mathcal{V}_0}\left[2\left(\frac{\partial\Psi(\mathbf{C}_{\mathrm{e}}^{\star})}{\partial\mathbf{C}_{\mathrm{e}}^{\star}} : \frac{\partial\mathbf{C}_{\mathrm{e}}^{\star}}{\partial\mathbf{C}^{\star}}\right) : \delta(\mathbf{C} + \tilde{\mathbf{C}}) - \tilde{\mathbf{C}} : \delta\mathbf{S} - \mathbf{S} : \delta\tilde{\mathbf{C}} \right]\mathrm{d}\mathcal{V}_0 - \delta\mathcal{W}^{\mathrm{ext}} = 0, \tag{21}$$

from which the following set of equations is obtained:

$$
\left.
\begin{aligned}
& \int_{\mathcal{V}_0} \left(\frac{\partial \Psi(\mathbf{C}_e^\star)}{\partial \mathbf{C}_e^\star} : \frac{\partial \mathbf{C}_e^\star}{\partial \mathbf{C}^\star} \right) : \delta \mathbf{C} \mathrm{d}\mathcal{V}_0 - \delta \mathcal{W}^{\mathrm{ext}} = 0 \\
& \frac{1}{2} \int_{\mathcal{V}_0} \left(\mathbf{S} - 2 \frac{\partial \Psi(\mathbf{C}_e^\star)}{\partial \mathbf{C}_e^\star} : \frac{\partial \mathbf{C}_e^\star}{\partial \mathbf{C}^\star} \right) : \delta \tilde{\mathbf{C}} \mathrm{d}\mathcal{V}_0 = 0, \qquad \frac{1}{2} \int_{\mathcal{V}_0} \tilde{\mathbf{C}} : \delta \mathbf{S} \mathrm{d}\mathcal{V}_0 = 0
\end{aligned}
\right\} .
$$

(22)

The strong form of Eq. $(22)_3$ leads to the relation $\tilde{\mathbf{C}} = \mathbf{0}$, which yields $\mathbf{C}^\star = \mathbf{C}$ and $\mathbf{C}_e^\star = \mathbf{C}_e$. From this result and the strong form of Eq. $(22)_2$, the constitutive equation for the second Piola–Kirchhoff stress $\mathbf{S}$ is obtained as follows:

$$
\mathbf{S} = 2 \frac{\partial \Psi(\mathbf{C}_e)}{\partial \mathbf{C}_e} : \frac{\partial \mathbf{C}_e}{\partial \mathbf{C}} = \mathbf{F}_g^{-1} \mathbf{S}_e \mathbf{F}_g^{-\top} \quad \text{with} \quad \mathbf{S}_e = 2 \frac{\partial \Psi(\mathbf{C}_e)}{\partial \mathbf{C}_e},
$$

(23)

and use has been made of Eq. $(10)_1$. Obviously, $\mathbf{S}_e$ is the push-forward of the material tensor $\mathbf{S}$ to the intermediate configuration.

As usual in the EAS-based finite element formulations, the stress $\mathbf{S}$ is assumed to be orthogonal to $\tilde{\mathbf{C}}$ over an element, giving $\int_{\mathcal{V}_0} \tilde{\mathbf{C}} : \mathbf{S} \mathrm{d}\mathcal{V}_0 = 0$. Accordingly, the first part of Eq. $(22)_2$ vanishes and Eq. $(22)_3$ will be identically satisfied. Thus, the following system of equations is obtained:

$$
\delta \mathcal{U}^{\mathrm{int}} - \delta W^{\mathrm{ext}} = 0, \quad \delta H = 0,
$$

(24)

where the expressions for $\delta \mathcal{U}^{\mathrm{int}}$ and δH are given by

$$
\delta H = \frac{1}{2} \int_{\mathcal{V}_0} \mathbf{S} : \delta \tilde{\mathbf{C}} \mathrm{d}\mathcal{V}_0, \quad \delta \mathcal{U}^{\mathrm{int}} = \frac{1}{2} \int_{\mathcal{V}_0} \mathbf{S} : \delta \mathbf{C} \mathrm{d}\mathcal{V}_0.
$$

(25)

The volume element $\mathrm{d}\mathcal{V}_0$, located at the elevation Z with respect to the reference midsurface is given by $\mathrm{d}\mathcal{V}_0 = Y \mathrm{d}\mathcal{A}_0 \mathrm{d}Z$, where $Y = \det(\mathbf{I} - Z\mathbf{K})$ and $\mathrm{d}\mathcal{A}_0 = \sqrt{A} \mathrm{d}\zeta^1 \mathrm{d}\zeta^2$ [58]. Here, $\mathrm{d}\mathcal{A}_0$ is an area element on $\mathcal{S}_0$, and $A = A_{11} A_{22} - A_{12}^2$ is the determinant of the covariant surface metric tensor on $\mathcal{S}_0$. By substituting Eq. (5) into $(25)_3$ one obtains the following expression for the virtual internal energy $\delta \mathcal{U}^{\mathrm{int}}$:

$$
\delta \mathcal{U}^{\mathrm{int}} = \frac{1}{2} \int_{\mathcal{S}_0} \left(\mathbf{N} : \delta \mathbf{C}^{[0]} + \mathbf{M} : \delta \mathbf{C}^{[1]} \right) \mathrm{d}\mathcal{A}_0 \quad \text{with} \quad \{\mathbf{N}, \mathbf{M}\} = \int_{-h/2}^{h/2} \{1, Z\} Y \mathbf{S} \mathrm{d}Z.
$$

(26)

Similarly, from Eqs. $(17)_2$ and $(26)_2$, the orthogonality condition may be rewritten as

$$
\delta H = \frac{1}{2} \int_{\mathcal{S}_0} \mathbf{N} : \delta \tilde{\mathbf{C}} \mathrm{d}\mathcal{A}_0 = 0.
$$

(27)

By back substituting Eq. (26) into (25)$_1$, the *enhanced form of virtual work principle* is obtained. The second equation is also given in (27). These two equations will be solved by the nonlinear finite element method in the next section. For linearisation purpose, the increment of the virtual internal energy and that of the orthogonality condition are calculated as follows:

$$
\left.
\begin{aligned}
\Delta\delta\mathcal{U}^{\text{int}} &= \frac{1}{2}\int_{S_0}\left(\Delta\mathbf{N}\!:\!\delta\mathbf{C}^{[0]} + \mathbf{N}\!:\!\Delta\delta\mathbf{C}^{[0]} + \Delta\mathbf{M}\!:\!\delta\mathbf{C}^{[1]} + \mathbf{M}\!:\!\Delta\delta\mathbf{C}^{[1]}\right)\mathrm{d}\mathcal{A}_0 \\
\Delta\delta H &= \frac{1}{2}\int_{S_0}\left(\Delta\mathbf{N}\!:\!\delta\tilde{\mathbf{C}} + \mathbf{N}\!:\!\Delta\delta\tilde{\mathbf{C}}\right)\mathrm{d}\mathcal{A}_0
\end{aligned}
\right\},
\tag{28}
$$

where $\Delta\mathbf{N}$ and $\Delta\mathbf{M}$ are given by

$$
\{\Delta\mathbf{N}, \Delta\mathbf{M}\} = \frac{1}{2}\left\{\boldsymbol{\mathcal{L}}^{[0]}\!:\!(\Delta\mathbf{C}^{[0]} + \Delta\tilde{\mathbf{C}}) + \boldsymbol{\mathcal{L}}^{[1]}\!:\!\Delta\mathbf{C}^{[1]}, \ \boldsymbol{\mathcal{L}}^{[1]}\!:\!(\Delta\mathbf{C}^{[0]} + \Delta\tilde{\mathbf{C}}) + \boldsymbol{\mathcal{L}}^{[2]}\!:\!\Delta\mathbf{C}^{[1]}\right\}.
\tag{29}
$$

Here, the fourth-order tensors $\boldsymbol{\mathcal{L}}^{[\mathcal{I}]}$ ($\mathcal{I} = 0, 1, 2$) are defined as follows:

$$
\boldsymbol{\mathcal{L}}^{[\mathcal{I}]} = \int_{-h/2}^{h/2} \mathcal{C}YZ^{\mathcal{I}}\mathrm{d}Z,
\tag{30}
$$

where the expression for the fourth-order tensor $\mathcal{C}$ is provided in the Appendix.

5. Finite element formulation

In this section, finite element formulation of the present shell model with growing mass is developed. The shell geometry in the reference configuration is discretized into N_{EL} elements, namely $\mathcal{B}_0 = \cup_{\mathcal{E}=1}^{N_{EL}}\mathcal{B}_0^{\mathcal{E}}$. Let the shell element $S_0^{\mathcal{E}}$ be the midsurface of $\mathcal{B}_0^{\mathcal{E}}$. The geometry and field quantities over $S_0^{\mathcal{E}}$ are interpolated via

$$
\{\mathbb{R}, \mathbb{u}, \mathbb{w}, \boldsymbol{\psi}\} = \sum_{\mathcal{I}=1}^{N_{ND}} P_{\mathcal{I}}(\zeta^1, \zeta^2)\{\mathbb{R}_{\mathcal{I}}, \mathbb{u}_{\mathcal{I}}, \mathbb{w}_{\mathcal{I}}, \boldsymbol{\psi}_{\mathcal{I}}\},
\tag{31}
$$

where $P_{\mathcal{I}}$ is $\mathcal{I}$th interpolation function and N_{ND} is the number of nodes in $S_0^{\mathcal{E}}$. The symbol $\mathbb{R}_{\mathcal{I}}$ denotes the position vector of the $\mathcal{I}$th node. Similar definitions hold for $\mathbb{u}_{\mathcal{I}}$, $\mathbb{w}_{\mathcal{I}}$, and $\boldsymbol{\psi}_{\mathcal{I}}$. Moreover, $\delta\mathbb{U}_{\mathcal{I}} = \{\delta\mathbb{u}_{\mathcal{I}}^{\mathsf{T}}, \delta\mathbb{w}_{\mathcal{I}}^{\mathsf{T}}, \delta\boldsymbol{\psi}_{\mathcal{I}}\}^{\mathsf{T}}$ and $\Delta\mathbb{U}_{\mathcal{I}} = \{\Delta\mathbb{u}_{\mathcal{I}}^{\mathsf{T}}, \Delta\mathbb{w}_{\mathcal{I}}^{\mathsf{T}}, \Delta\boldsymbol{\psi}_{\mathcal{I}}\}^{\mathsf{T}}$ are, respectively, the virtual and incremental generalized displacement vectors at the $\mathcal{I}$th node of the element.

In the next step, the deformation measures $\mathbf{C}^{[\mathcal{J}]}$ ($\mathcal{J} = 0, 1$) defined in Eqs. (5) and (6) are written in vectorial form, namely $\mathbb{C}^{[\mathcal{J}]} = \{C_{11}^{[\mathcal{J}]}, C_{22}^{[\mathcal{J}]}, C_{33}^{[\mathcal{J}]}, 2C_{23}^{[\mathcal{J}]}, 2C_{13}^{[\mathcal{J}]}, 2C_{12}^{[\mathcal{J}]}\}^{\mathsf{T}}$. The variation and increment of $\mathbb{C}^{[\mathcal{J}]}$ may be written as

$$\{\delta\mathbb{C}^{[\mathcal{J}]}, \Delta\mathbb{C}^{[\mathcal{J}]}\} = 2\sum_{\mathcal{I}=1}^{N_{ND}} \mathbb{B}_{\mathcal{I}}^{[\mathcal{J}]}\{\delta\mathbb{U}_{\mathcal{I}}, \Delta\mathbb{U}_{\mathcal{I}}\}, \tag{32}$$

where the matrices $\mathbb{B}_{\mathcal{I}}^{[\mathcal{J}]}$ ($\mathcal{J} = 0, 1$) are as follows:

$$\mathbb{B}_{\mathcal{I}}^{[0]} = \begin{bmatrix} P_{\mathcal{I},1}\mathbb{a}_1^{\mathsf{T}} & \mathbf{0}_{1\times 3} & 0 \\ P_{\mathcal{I},2}\mathbb{a}_2^{\mathsf{T}} & \mathbf{0}_{1\times 3} & 0 \\ \mathbf{0}_{1\times 3} & P_{\mathcal{I}}\mathbb{a}_3^{\mathsf{T}} & 0 \\ P_{\mathcal{I},2}\mathbb{a}_3^{\mathsf{T}} & P_{\mathcal{I}}\mathbb{a}_2^{\mathsf{T}} & 0 \\ P_{\mathcal{I},1}\mathbb{a}_3^{\mathsf{T}} & P_{\mathcal{I}}\mathbb{a}_1^{\mathsf{T}} & 0 \\ \mathbb{p}^{\mathsf{T}} & \mathbf{0}_{1\times 3} & 0 \end{bmatrix}, \quad \mathbb{B}_{\mathcal{I}}^{[1]} = \begin{bmatrix} P_{\mathcal{I},1}\mathbb{a}_{3,1}^{\mathsf{T}} & P_{\mathcal{I},1}\mathbb{a}_1^{\mathsf{T}} & 0 \\ P_{\mathcal{I},2}\mathbb{a}_{3,2}^{\mathsf{T}} & P_{\mathcal{I},2}\mathbb{a}_2^{\mathsf{T}} & 0 \\ \mathbf{0}_{1\times 3} & 4\psi P_{\mathcal{I}}\mathbb{a}_3^{\mathsf{T}} & 2P_{\mathcal{I}}\mathbb{a}_3^{\mathsf{T}}\mathbb{a}_3 \\ 2\psi P_{\mathcal{I},2}\mathbb{a}_3^{\mathsf{T}} & \mathbb{q}_2^{\mathsf{T}} & 2P_{\mathcal{I}}\mathbb{a}_3^{\mathsf{T}}\mathbb{a}_2 \\ 2\psi P_{\mathcal{I},1}\mathbb{a}_3^{\mathsf{T}} & \mathbb{q}_1^{\mathsf{T}} & 2P_{\mathcal{I}}\mathbb{a}_3^{\mathsf{T}}\mathbb{a}_1 \\ P_{\mathcal{I},2}\mathbb{a}_{3,1}^{\mathsf{T}} + P_{\mathcal{I},1}\mathbb{a}_{3,2}^{\mathsf{T}} & \mathbb{p}^{\mathsf{T}} & 0 \end{bmatrix}. \tag{33}$$

Here, the vectors $\mathbb{p}$ and $\mathbb{q}_\alpha$ ($\alpha = 1, 2$) are given by

$$\mathbb{p} = P_{\mathcal{I},2}\mathbb{a}_1 + P_{\mathcal{I},1}\mathbb{a}_2, \quad \mathbb{q}_\alpha = 2\psi P_{\mathcal{I}}\mathbb{a}_\alpha + (P_{\mathcal{I}}\mathbb{a}_3)_{,\alpha}. \tag{34}$$

Motivated by Eqs. (5) and (6), the enhancement tensor is written as $\tilde{\mathbf{C}} = \tilde{C}_{ij}\mathbf{G}^i \otimes \mathbf{G}^j$. The vectorial form of $\tilde{\mathbf{C}}$ is denoted here by $\tilde{\mathbb{C}}$ and its structure is similar to $\mathbb{C}^{[\mathcal{J}]}$ ($\mathcal{J} = 0, 1$) as introduced above. In the present formulation, it is assumed that $\tilde{\mathbb{C}}$, $\delta\tilde{\mathbb{C}}$, and $\Delta\tilde{\mathbb{C}}$ are given by

$$\{\tilde{\mathbb{C}}, \delta\tilde{\mathbb{C}}, \Delta\tilde{\mathbb{C}}\} = 2\tilde{\mathbb{B}}\{\mathbb{c}_{\mathcal{E}}, \delta\mathbb{c}_{\mathcal{E}}, \Delta\mathbb{c}_{\mathcal{E}}\} \quad \text{with} \quad \tilde{\mathbb{B}} = \frac{\tilde{J}_0}{\tilde{J}}\bar{\mathbb{B}}(\xi^1, \xi^2), \tag{35}$$

where $\tilde{J}$ is the Jacobian of the mapping from the parent element in the nondimensional $\xi^1\xi^2$ space (with $\xi^1, \xi^2 \in [-1, 1]$) to the shell element $\mathcal{S}_0^{\mathcal{E}}$ in the physical space. Additionally, $\tilde{J}_0$ is the value of $\tilde{J}$ evaluated at the element center with $\xi^1 = \xi^2 = 0$. Furthermore, $\bar{\mathbb{B}}$ is an interpolation matrix, and $\mathbb{c}_{\mathcal{E}}$ is the vector of enhanced parameters. In this work, the basic shell element employed in the simulations has four nodes. For this element, following Sansour [58], a

14-parameter enhanced formulation is considered. Accordingly, the 6×14 matrix $\tilde{\mathbb{B}}$ is given by

$$
\tilde{\mathbb{B}} = \begin{bmatrix}
\xi^1 & \xi^1\xi^2 & 0 & 0 & 0 & 0 & 0 & 0 & 0 & 0 & 0 & 0 & 0 & 0 \\
0 & 0 & \xi^2 & \xi^1\xi^2 & 0 & 0 & 0 & 0 & 0 & 0 & 0 & 0 & 0 & 0 \\
0 & 0 & 0 & 0 & \xi^1 & \xi^2 & \xi^1\xi^2 & 0 & 0 & 0 & 0 & 0 & 0 & 0 \\
0 & 0 & 0 & 0 & 0 & 0 & 0 & \xi^2 & \xi^1\xi^2 & 0 & 0 & 0 & 0 & 0 \\
0 & 0 & 0 & 0 & 0 & 0 & 0 & 0 & 0 & \xi^1 & \xi^1\xi^2 & 0 & 0 & 0 \\
0 & 0 & 0 & 0 & 0 & 0 & 0 & 0 & 0 & 0 & 0 & \xi^1 & \xi^2 & \xi^1\xi^2
\end{bmatrix}.
\tag{36}
$$

The enhanced form of virtual work principle expressed in Eq. (25)$_1$ and the orthogonality condition (27) over the element $\mathcal{B}_0^{\mathcal{E}}$ are now written in the following discretized forms:

$$
\delta \mathcal{W}^{\text{ext}} - \delta \mathcal{U}^{\text{int}} = \sum_{\mathcal{I}=1}^{N_{ND}} \delta \mathbb{U}_{\mathcal{I}}^{\top} (\mathbb{f}_{\mathcal{I}}^{\text{ext}} - \mathbb{f}_{\mathcal{I}}^{\text{int}}) = 0, \quad \delta H = \delta \mathbb{c}^{\top} \mathbb{h} = 0,
\tag{37}
$$

where $\mathbb{f}_{\mathcal{I}}^{\text{ext}}$ is the nodal generalized external force vector, which can be easily determined based upon the type of loading applied to the shell. Moreover, the nodal internal force vector $\mathbb{f}_{\mathcal{I}}^{\text{int}}$, and the orthogonality vector $\mathbb{h}$ of the element are as follows:

$$
\mathbb{f}_{\mathcal{I}}^{\text{int}} = \int_{\mathcal{S}_0^{\mathcal{E}}} \left(\mathbb{B}_{\mathcal{I}}^{[0]\top} \mathbb{N} + \mathbb{B}_{\mathcal{I}}^{[1]\top} \mathbb{M} \right) d\mathcal{A}_0, \quad \mathbb{h} = \int_{\mathcal{S}_0^{\mathcal{E}}} \tilde{\mathbb{B}}^{\top} \mathbb{N} \, d\mathcal{A}_0 = \mathbf{0},
\tag{38}
$$

where $\mathbb{N}$ and $\mathbb{M}$ are the vectorial representations of $\mathbf{N}$ and $\mathbf{M}$, respectively. Since the virtual generalized displacement vector $\delta \mathbb{U}$ and the vector of virtual enhanced parameters $\delta \mathbb{c}$ are arbitrary, from Eqs. (37) the system of nonlinear algebraic equations $\mathbb{f}_{\mathcal{I}}^{\text{ext}} - \mathbb{f}_{\mathcal{I}}^{\text{int}} = \mathbf{0}$ ($\mathcal{I} = 1, 2, ..., N_{ND}$) and $\mathbb{h} = \mathbf{0}$ over the shell element $\mathcal{S}_0^{\mathcal{E}}$ ($\mathcal{E} = 1, 2, ..., N_{EL}$) are obtained. To solve the equations via Newton–Raphson method, from Eqs. (28), (29), (34) and (35), the following linearized form of equations are obtained:

$$
\left.
\begin{aligned}
\sum_{\mathcal{I}=1}^{N_{ND}} \delta \mathbb{U}_{\mathcal{I}}^{\top} \left(\sum_{\mathcal{J}=1}^{N_{ND}} \mathbb{K}_{\mathcal{I}\mathcal{J}}^{\mathbf{uu}} \Delta \mathbb{U}_{\mathcal{J}} + \mathbb{K}_{\mathcal{I}}^{\mathbf{uc}} \Delta \mathbb{c} \right) = \sum_{\mathcal{I}=1}^{N_{ND}} \delta \mathbb{U}_{\mathcal{I}}^{\top} (\mathbb{f}_{\mathcal{I}}^{\text{ext}} - \mathbb{f}_{\mathcal{I}}^{\text{int}}) \\
\delta \mathbb{c}^{\top} \left(\sum_{\mathcal{I}=1}^{N_{ND}} \mathbb{K}_{\mathcal{I}}^{\mathbf{cu}} \Delta \mathbb{U}_{\mathcal{I}} + \mathbb{K}^{\mathbf{cc}} \Delta \mathbb{c} \right) = -\delta \mathbb{c}^{\top} \mathbb{h}
\end{aligned}
\right\},
\tag{39}
$$

where the matrices $\mathbb{K}_{\mathcal{I}}^{\mathbf{uc}}$, $\mathbb{K}_{\mathcal{I}}^{\mathbf{cu}}$ and $\mathbb{K}^{\mathbf{cc}}$ are given by

$$
\mathbb{K}_{\mathcal{I}}^{\mathbf{uc}} = (\mathbb{K}_{\mathcal{I}}^{\mathbf{cu}})^{\top} = \int_{\mathcal{S}_0^{\mathcal{E}}} \left(\mathbb{B}_{\mathcal{I}}^{[0]\top} \mathbb{L}^{[0]} + \mathbb{B}_{\mathcal{I}}^{[1]\top} \mathbb{L}^{[1]} \right) \tilde{\mathbb{B}} d\mathcal{A}_0, \quad \mathbb{K}^{\mathbf{cc}} = \int_{\mathcal{S}_0^{\mathcal{E}}} \tilde{\mathbb{B}}^{\top} \mathbb{L}^{[0]} \tilde{\mathbb{B}} d\mathcal{A}_0.
\tag{40}
$$

Moreover, the matrix $\mathbb{K}_{IJ}^{\mathbf{uu}}$ can be decomposed into the material and geometric parts, namely $\mathbb{K}_{IJ}^{\mathbf{uu}} = \mathbb{K}_{IJ}^{\mathbf{uu(mat)}} + \mathbb{K}_{IJ}^{\mathbf{uu(geo)}}$. The expression for $\mathbb{K}_{IJ}^{\mathbf{uu(mat)}}$ may be written as

$$\mathbb{K}_{IJ}^{\mathbf{uu(mat)}} = \int_{S_0^{\mathcal{E}}} \left(\mathbb{B}_I^{[0]\top} \mathbb{L}^{[0]} \mathbb{B}_J^{[0]} + \mathbb{B}_I^{[0]\top} \mathbb{L}^{[1]} \mathbb{B}_J^{[1]} + \mathbb{B}_I^{[1]\top} \mathbb{L}^{[1]} \mathbb{B}_J^{[0]} + \mathbb{B}_I^{[1]\top} \mathbb{L}^{[2]} \mathbb{B}_J^{[1]} \right) \mathrm{d}\mathcal{A}_0. \tag{41}$$

It is noted that in Eqs. (40) and (41), the quantities denoted by $\mathbb{L}^{[I]}$ ($I = 0, 1, 2$) are the 6×6 matrix forms of $\mathcal{L}^{[I]}$. The geometric contribution may be also decomposed as $\mathbb{K}_{IJ}^{\mathbf{uu(geo)}} = \mathbb{K}_{IJ}^{\mathbf{uu(gN)}} + \mathbb{K}_{IJ}^{\mathbf{uu(gM)}}$, with

$$\mathbb{K}_{IJ}^{\mathbf{uu(gN)}} = \int_{S_0^{\mathcal{E}}} \begin{bmatrix} b_1 \mathbb{i} & b_2 \mathbb{i} & \mathbf{0}_{3\times 1} \\ b_3 \mathbb{i} & b_4 \mathbb{i} & \mathbf{0}_{3\times 1} \\ \mathbf{0}_{1\times 3} & \mathbf{0}_{1\times 3} & 0 \end{bmatrix} \mathrm{d}\mathcal{A}_0, \tag{42}$$

$$\mathbb{K}_{IJ}^{\mathbf{uu(gM)}} = \int_{S_0^{\mathcal{E}}} \begin{bmatrix} \mathbf{0}_{3\times 3} & (k_1 + 2\psi k_2)\mathbb{i} & 2k_2 \mathbb{a}_3 \\ (k_1 + 2\psi k_3)\mathbb{i} & k_4 \mathbb{i} & 2P_I P_J \mathbb{z} \\ 2k_3 \mathbb{a}_3^\top & 2P_I P_J \mathbb{z}^\top & 0 \end{bmatrix} \mathrm{d}\mathcal{A}_0, \tag{43}$$

where $\mathbb{i}$ is the 3×3 identity matrix. Moreover, the quantities denoted by b_I and k_I ($I = 1, 2, ..., 4$), and the vector $\mathbb{z}$ are as follows:

$$\left. \begin{aligned} \{b_1, k_1\} = \mathbb{Q}_I^\top \{\mathbb{N}^{[\mathrm{p}]}, \mathbb{M}^{[\mathrm{p}]}\} \mathbb{Q}_J, \quad \{b_2, k_2\} = \mathbb{Q}_I^\top \{\mathbb{N}^{[\mathrm{s}]}, \mathbb{M}^{[\mathrm{s}]}\} P_J \\ \{b_3, k_3\} = \mathbb{Q}_J^\top \{\mathbb{N}^{[\mathrm{s}]}, \mathbb{M}^{[\mathrm{s}]}\} P_I, \quad b_4 = P_I P_J \mathbb{D} \mathbf{N} \mathbb{D} \\ k_4 = k_2 + k_3 + 4\psi P_I P_J \mathbb{D} \mathbf{M} \mathbb{D}, \quad \mathbb{z} = \mathbb{a}_\alpha (\mathbb{M}^{[\mathrm{s}]})^\alpha + 2\mathbb{a}_3 \mathbb{D} \mathbf{M} \mathbb{D} \end{aligned} \right\}. \tag{44}$$

Here, $\mathbb{Q}_I = \{P_{I,1}, P_{I,2}\}^\top$ is a 2×1 vector that involves the partial derivatives of the interpolation function P_I. Additionally, $\mathbb{N}^{[\mathrm{p}]}$ and $\mathbb{M}^{[\mathrm{p}]}$ are the 2×2 matrices that contain the planar components of $\mathbf{N}$ and $\mathbf{M}$, respectively. Furthermore, $\mathbb{N}^{[\mathrm{s}]}$ and $\mathbb{M}^{[\mathrm{s}]}$ are, respectively, the 2×1 vectors that contain the out-of plane shear components of $\mathbf{N}$ and $\mathbf{M}$. It is also noted that $(\mathbb{M}^{[\mathrm{s}]})^\alpha$ is the α'th component of $\mathbb{M}^{[\mathrm{s}]}$. From Eq. (39), the following system of linear equations is obtained:

$$\begin{bmatrix} \mathbb{K}^{\mathbf{uu}} & \mathbb{K}^{\mathbf{uc}} \\ \mathbb{K}^{\mathbf{uc}\top} & \mathbb{K}^{\mathbf{cc}} \end{bmatrix} \begin{Bmatrix} \Delta \mathbb{U} \\ \Delta \mathbb{c} \end{Bmatrix} = \begin{Bmatrix} \mathbb{f}^{\mathrm{ext}} - \mathbb{f}^{\mathrm{int}} \\ -\mathbb{h} \end{Bmatrix}, \tag{45}$$

where $\mathbb{K}^{\mathbf{uu}}$ is a matrix whose $\mathcal{IJ}$th block is $\mathbb{K}^{\mathbf{uu}}_{\mathcal{IJ}}$. Similarly, the $\mathcal{I}$th block of $\mathbb{K}^{\mathbf{uc}}$, $\mathbb{f}^{int}$ and $\mathbb{f}^{ext}$ are $\mathbb{K}^{\mathbf{uc}}_{\mathcal{I}}$, $\mathbb{f}^{int}_{\mathcal{I}}$ and $\mathbb{f}^{ext}_{\mathcal{I}}$, respectively. Next, the incremental vector of enhanced parameters, $\Delta \mathbb{c}$, is eliminated at the element level, from which the linear matrix equation $\mathbb{K}\Delta\mathbb{U} = -\mathbb{F}$, with $\mathbb{K} = \mathbb{K}^{\mathbf{uu}} - \mathbb{K}^{\mathbf{uc}}\mathbb{K}^{\mathbf{cc}-1}\mathbb{K}^{\mathbf{uc}\mathsf{T}}$ and $\mathbb{F} = \mathbb{f}^{int} - \mathbb{f}^{ext} - \mathbb{K}^{\mathbf{uc}}\mathbb{K}^{\mathbf{cc}-1}\mathbb{h}$ is obtained. Finally, the assembled system of equations may be written as $\mathbb{A}^{N_{EL}}_{\mathcal{E}=1}\mathbb{K}\Delta\mathbb{U} = -\mathbb{A}^{N_{EL}}_{\mathcal{E}=1}\mathbb{F}$, where $\mathbb{A}^{N_{EL}}_{\mathcal{E}=1}$ is the assembly operator.

Next, from Eq. (23), it observed that the growth part of deformation gradient $\mathbf{F}_\mathfrak{g}$, and hence the growth parameter $\theta_\mathfrak{g}$ is needed to calculate the stress tensor $\mathbf{S}$. The stress tensor is used to calculate the force resultant $\mathbf{N}$, the moment resultant $\mathbf{N}$, and even the fourth-order tensor $\boldsymbol{C}$. In particular, the internal force $\mathbb{f}^{int}$ and the element stiffness matrix $\mathbb{K}$ will be dependent upon the growth parameter $\theta_\mathfrak{g}$. Accordingly, it is important to calculate $\theta_\mathfrak{g}$ at all Gauss points of all elements by solving the evolution equation (15). A wide variety of methods including the unconditionally stable *Euler backward* differentiation scheme may be employed for this purpose. Accordingly, at each Gauss point, let $\theta^{n+1}_\mathfrak{g}$ and $\theta^n_\mathfrak{g}$ be the values of $\theta_\mathfrak{g}$ at the times t_{n+1} and t_n, respectively. Presuming $\theta_e > \theta^{crit}_e$, or equivalently $\Phi_2 > 0$, the expression for $\dot{\theta}_\mathfrak{g}$ in Eq. (15) at the time t_{n+1} is approximated as follows:

$$\dot{\theta}^{n+1}_\mathfrak{g} = \frac{\theta^{n+1}_\mathfrak{g} - \theta^n_\mathfrak{g}}{\Delta t} = \beta(\theta^{n+1}_\mathfrak{g}, \theta^{n+1}), \tag{46}$$

where $\Delta t = t_{n+1} - t_n$ is the time increment. To solve Eq. (46) for $\theta^{n+1}_\mathfrak{g}$ by Newton method, it is rewritten as

$$R^{n+1} = \theta^{n+1}_\mathfrak{g} - \theta^n_\mathfrak{g} - \Delta t\beta(\theta^{n+1}_\mathfrak{g}, \theta^{n+1}) = 0, \tag{47}$$

from which the new value of $\theta^{n+1}_\mathfrak{g}$ is obtained via the following relation:

$$\theta^{n+1}_{\mathfrak{g}(new)} = \theta^{n+1}_{\mathfrak{g}(old)} - \frac{R^{n+1}_{(old)}}{K} \quad \text{with} \quad K = \left(\frac{\partial R}{\partial \theta_\mathfrak{g}}\right)^{n+1}_{(old)} = 1 - \Delta t\left(\frac{\partial\beta}{\partial\theta_\mathfrak{g}}\right)^{n+1}_{(old)}. \tag{48}$$

Here, the indices "old" and "new" refer to Newton iterations at the time t_{n+1}. Moreover, from Eqs. (15) and (16), the expression for $\frac{\partial\beta}{\partial\theta_\mathfrak{g}}$ is given by

$$\frac{\partial\beta}{\partial\theta_\mathfrak{g}} = \frac{\partial\Phi_1}{\partial\theta_\mathfrak{g}}\Phi_2 + \Phi_1\frac{\partial\Phi_2}{\partial\theta_\mathfrak{g}} = -\left(\frac{\gamma\Phi_2}{\theta^{max}_\mathfrak{g} - \theta_\mathfrak{g}} + \frac{\theta}{\theta^2_\mathfrak{g}}\right)\Phi_1. \tag{49}$$

The iteration procedure terminates if $|\theta^{n+1}_{\mathfrak{g}(new)} - \theta^{n+1}_{\mathfrak{g}(old)}| < \epsilon$, where ϵ is a sufficiently small number.

6. Numerical examples

To investigate the applicability of the proposed formulation, several numerical examples are presented in this section. An in-house FE code based on the developed formulation has been prepared. The integrals over the element surface are evaluated by the 2×2 Gauss–Legendre integration rule. Additionally, to integrate along the shell thickness, namely, in the Z-direction, three Gauss points are considered.

6.1. Growth of a pinched thin-walled cylinder

In this example, the growth of a hollow cylinder made of soft materials under mechanical loading is investigated. The referential average radius, thickness, and length of the cylinder are $\{R, h, L\} = \{9, 0.2, 30\}$ cm, respectively. Following Ref. [66], the strain energy density of the form $\Psi(\mathbf{C_e}) = \frac{1}{2}[\mu(\operatorname{tr}\mathbf{C_e} - 3 - 2\ln J_e) + \lambda \ln^2 J_e]$ is considered. Here, λ and μ are Lamé constants, and the relation $\lambda = 2\nu\mu/(1 - 2\nu)$, with ν as Poisson's ratio, holds. In Ref. [66], the values of $\mu = 6 \times 10^4$ MPa and $\nu = 0.4$ have been employed. However, to model soft tissues, the shear modulus has been reduced to $\mu = 2$ MPa in Rausch and Kuhl [52].

Due to symmetry, the part shown by the points $\{A, B, C, D\}$ in Fig. 3(**a**) as one-eights of the cylinder is discretized by the shell elements. In the loading stage, the line AD is moved gradually 87 mm in $-X_3$ direction during $t_{\mathfrak{l}} = 1$ s. The line AD is held fixed for $t_{\mathfrak{l}} = 30$ s to observe the growth phenomenon in the cylinder. After that, the external load is completely removed in $t_{\mathfrak{u}} = 1$ s.

Numerical simulations show that a mesh of 12×12 elements leads to convergent results. However, a mesh of 16×16 elements is used to obtain smoother deformed shapes. The nondimensional displacement components at the material points A and H versus the nondimensional time $t/t_{\max}$ are displayed in Fig. 3(**a**). It is noted that the material point H lies exactly between A and B. The vertical displacement of the point A at the end of the unloading stage is 33.1 mm. Next, the deformed shapes of the cylinder at four stages, namely at $t \in \{1, 16, 31, 32\}$ (s) are demonstrated in Fig. 3(**b–e**). The contour plots of the growth parameter $\theta_{\mathfrak{g}}$ are also displayed on the deformed shapes. Comparison of Figs. 3(**b**) and 3(**d**) shows that the contour plot of $\theta_{\mathfrak{g}}$ at the end of the growth stage obtained by the present formulation is in good agreement with that reported by Rausch and Kuhl [52]. The minor difference between the present work and that of Ref. [52] comes from the fact that the assumption of $F_{13} = F_{31} = F_{23} = F_{32} = 0$, for the components of the deformation gradient tensor, has been made in that reference (please see Remark 1 in [52]). However, from Eq. (4) it is obvious that all components of the deformation gradient are nonzero in the present formulation.

6.2. Growth of a square sheet with a circular hole

In this example, uniaxial stretching and the growth of a square sheet containing a circular hole are investigated. Following Ref. [67], the length and thickness of the square and the radius of the hole are $L = 20''$, $h = 0.1''$, and $R = 3''$, respectively. Moreover, it is assumed that the strain energy density obeys the compressible Mooney–Rivlin
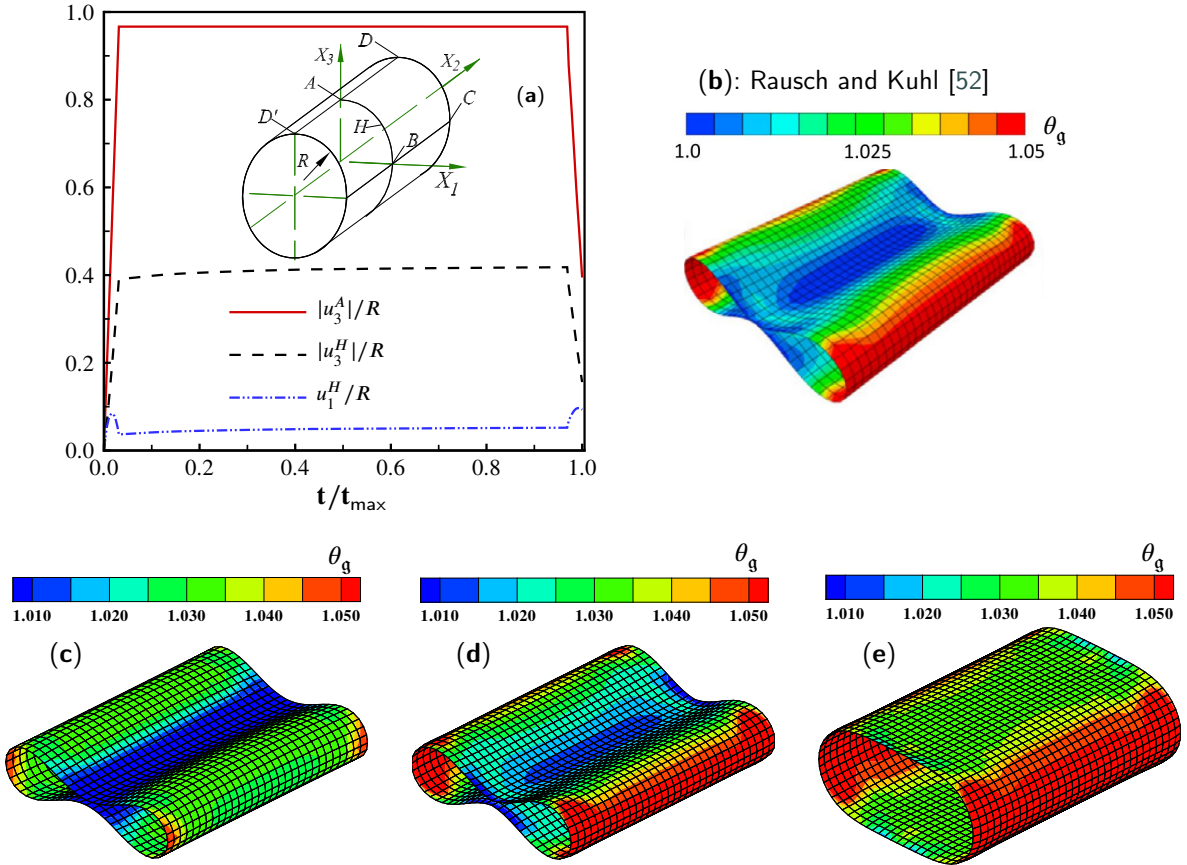
Figure 3: Growth of the pinched cylinder: history of displacement at the points A and H (**a**), deformed shape and the contour plot of $\theta_\mathfrak{g}$ at the end of growth stage taken from Rausch and Kuhl [52](**b**), end of loading stage (**c**), grown stage (**d**), unloaded stage (**e**).

material model of the form

$$\Psi(\mathbf{C}_e) = c_1(I_1^e - 3) + c_2(I_2^e - 3) - (\mu + 2c_2)\ln J_e + \tfrac{1}{2}(\lambda - 4c_2)\ln^2 J_e.$$

Here, I_1^e and I_2^e are the first two invariants of $\mathbf{C}_e$. The material constants of the model are $c_1 = 25$ (psi), $c_2 = 7$ (psi), and $v = 0.48$. It is noted that the shear modulus is given by the relation $\mu = 2(c1 + c2) = 64$ psi $= 0.44$ MPa. As usual, the relation $\lambda = 2v\mu/(1 - 2v)$ can be used to calculate the second Lamé constant. To model the growth effects in the sheet, following Ref. [39], the growth parameters are considered to be $\theta_\mathfrak{g}^{\max} = 2.4$, $\gamma = 2$, $T = 1$, and $\theta_e^{\text{crit}} = 1.01$.

As shown in Fig. 4(**a**), the pure elastic axial stretch $\lambda = 2$ is applied in the X_2-direction for $t_\mathfrak{l} = 1$ s. The top edge is then held fixed for $t_\mathfrak{g} = 20$ s to observe the growth in the sheet. Finally, the unloading is performed during $t_\mathfrak{u} = 1$ s. Accordingly, the entire time of simulation is $t_{\max} = 22$ s. Due to symmetry, only one-quarter of the sheet is discretized by the shell elements. It is noted that to achieve the initial elastic stretch $\lambda = 2$, the vertical deflection $V_{\max} = 10''$
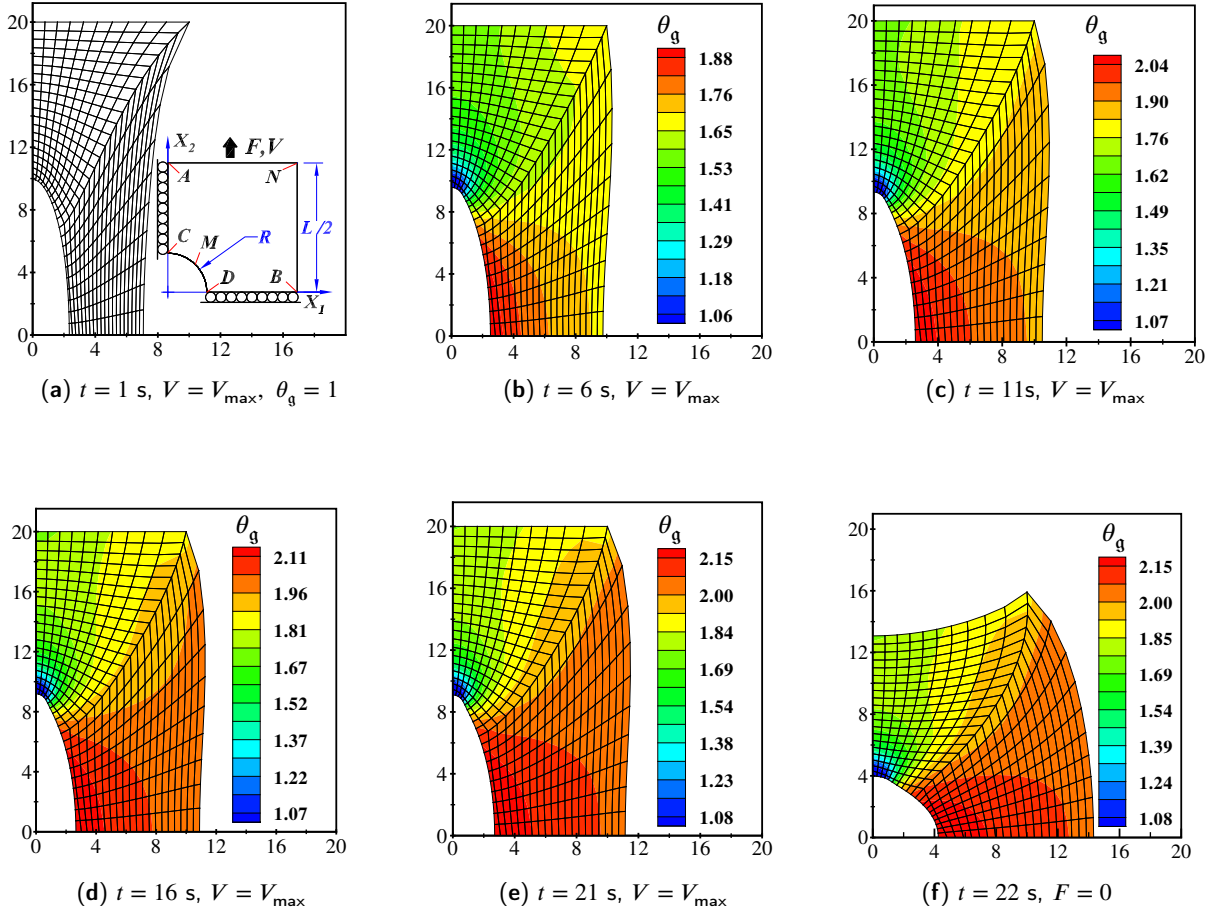
Figure 4: Deformed shapes of the sheet with the contour plots of the growth multiplier $\theta_\mathfrak{g}$ at different times.

has to be applied on the top edge of the model. Convergence analysis reveals that a mesh of 8×8 elements, as the number of elements, respectively, in the radial and circumferential directions of the circular hole, is sufficient to obtain mesh-independent results. However, a mesh of 20×20 elements is used to obtain smoother deformed shapes.

The deformed shapes of the sheet for $t \in \{1, 6, 11, 16, 21, 22\}$ s are displayed in Fig. 4. The deformed shape at the end of elastic loading is demonstrated in Fig. 4(**a**), where the growth multiplier is still $\theta_\mathfrak{g} = 1$ on the entire geometry. For $1 < t \leq 21$ s, the growth multiplier $\theta_\mathfrak{g}$ increases in the sheet. For $21 \leq t \leq 22$ s, the load on the top edge is gradually decreased to zero. The final grown geometry, corresponding to $t = 22$ s, is displayed in Fig. 4(**f**).

The time evolution of the growth parameter $\theta_\mathfrak{g}$, for the material points $\{A, B, C, D, M, N\}$, and the area ratio A/A_0 are displayed in Fig. 5(**a**). Moreover, the time history of the non-dimensional von Mises stress $\bar{\sigma}/\mu$, for the material points $\{A, B, C, D, M, N\}$, and the resultant vertical force F on the top edge of the one-quarter model are demonstrated in Fig. 5(**b**). The mentioned material points are shown in Fig. 4(**a**). It is noted that the curve corresponding to the applied
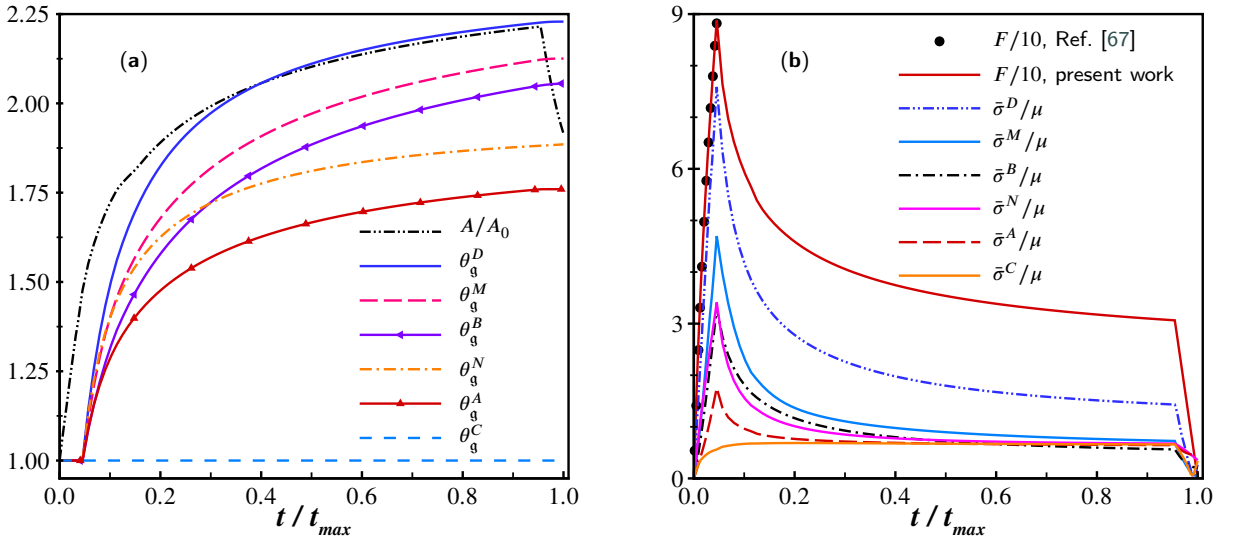
Figure 5: (a) Time evolution of A/A_0 and $\theta_{\mathfrak{g}}$ (at some material points), (b): time history of the applied force F and the non-dimensional von Mises stress $\bar{\sigma}/\mu$ (at some material points).
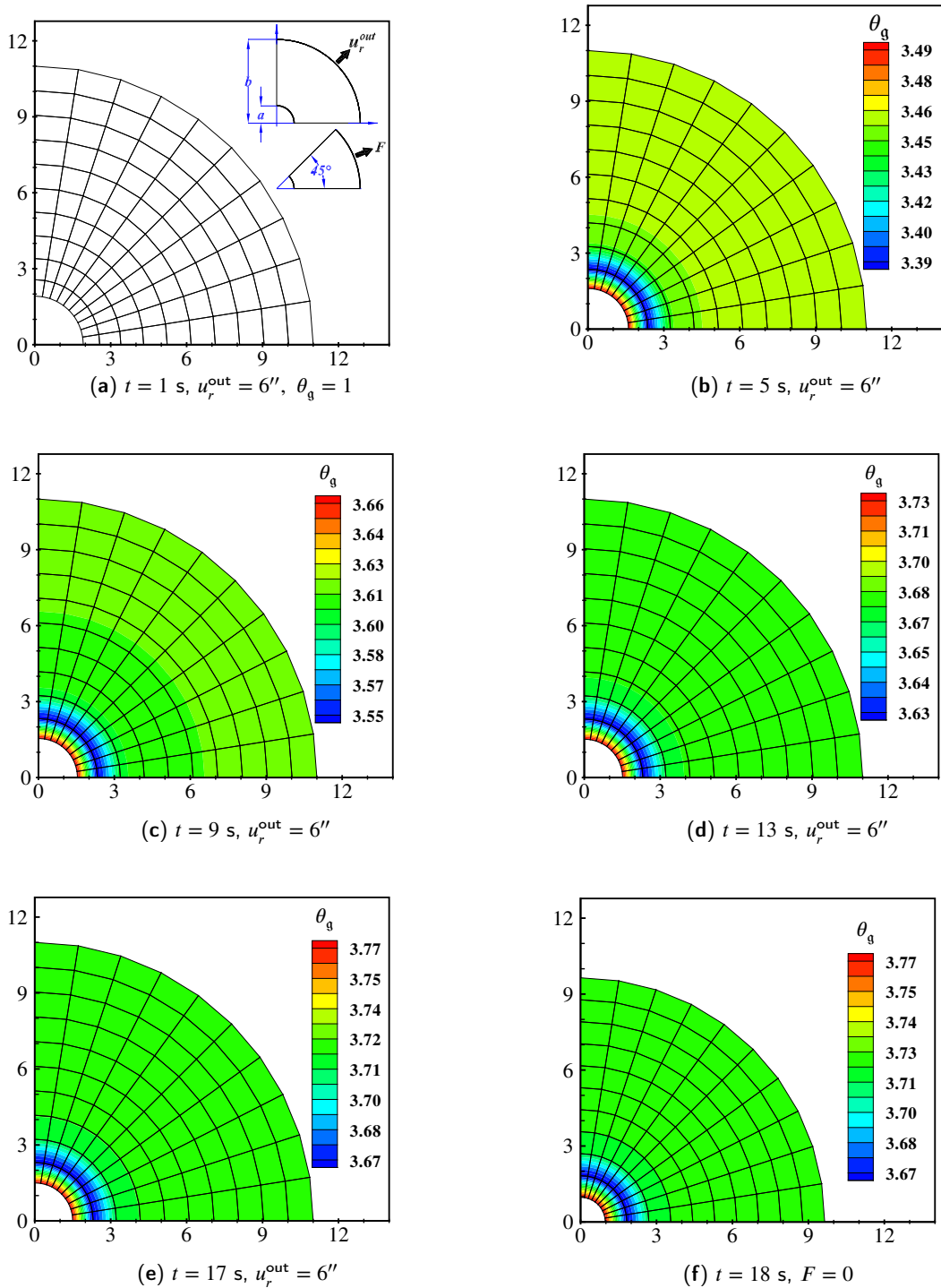
force F is coincident with that obtained by Ref. [67] for $t \in [0, 1]$. Additionally, the applied force F reduces during the growth processes. The same holds about the von Mises stress $\bar{\sigma}$, which indicates the stress relaxation behavior of the sheet in the growth stage. The point C, with the initial coordinates $(0, R)$, does not experience any growth during the entire process. Furthermore, the von Mises stress attains its minimum values at this point. On the other hand, the maximum growth parameter $\theta_{\mathfrak{g}}$ and the maximum von Mises stress are both observed at the material point D with the initial coordinates $(R, 0)$. The maximum value of the area stretch is $A_{\max}/A_0 = 2.1809$, which occurs at $t = 21$ s. After the unloading process, the final value of the area stretch is obtained to be $A_{\mathrm{f}}/A_0 = 1.9155$.

6.3. Growth of a soft tissue as an annular plate

In this example, the growth of a soft tissue whose geometry is an annular plate is simulated. Following Ref. [67], the inner and outer radii of the undeformed plate are $a = 0.5''$ and $b = 5''$, respectively. The initial thickness is also considered to be $h = 0.0625''$. Moreover, similar to example 6.2, it is assumed that the material obeys the compressible Mooney–Rivlin model. However, the constants of the model are $v = 0.48$, $c_1 = 18.35$ (psi), and $c_2 = 1.468$ (psi). Accordingly, the shear modulus is calculated to be $\mu = 0.27$ MPa. Following Ref. [43], the growth parameters are considered to be $\theta_{\mathfrak{g}}^{\max} = 4$, $\gamma = 2$, $T = \frac{1}{12}$ s, and $\theta_{\mathfrak{e}}^{\mathrm{crit}} = 1.21$. The radial displacement is applied from $u_r^{\mathrm{out}} = 0$ to the maximum value $(u_r^{\mathrm{out}})_{\max} = 6''$ is applied gradually on the outer radius of the sheet in $t_{\mathfrak{l}} = 1$ s. The maximum radial displacement is then held constant for $t_{\mathfrak{g}} = 16$ s to observe the growth in the sheet. In the last stage, the unloading procedure is performed during $t_{\mathfrak{u}} = 1$ s. It then follows that the maximum time of simulation is $t_{\max} = 18$ s.

Due to symmetry, only one-quarter of the annular plate is discretized by the shell elements. Numerical experiments reveal that a mesh of 6×6 elements, in radial and circumferential directions, is sufficient to achieve converged results. However, a mesh of 10×10 shell elements is used to obtain smoother deformed shapes. The deformed shapes of the full model for $t \in \{1, 5, 9, 13, 17, 18\}(s)$ are demonstrated in Fig. 6. The deformed shape at the end of elastic loading, corresponding to the time $t = 1$ s is displayed in Fig. 6(**a**), where the growth multiplier is still $\theta_{\mathfrak{g}} = 1$ on the entire geometry. As can be observed from Figs. 6(**b–e**), by increasing the time in the interval $1 < t \le 17$, the inner radius decreases, while the growth multiplier $\theta_{\mathfrak{g}}$ follows an increasing trend. The final grown geometry is illustrated in Fig. 6(**f**). After unloading, both inner and outer radii decrease.

Time evolution of the radial displacements u_r^{in} and u_r^{out}, area stretch A/A_0, and the resultant force F are displayed in Fig. 7(**a**). Moreover, the time history of the non-dimensional von Mises stress $\bar{\sigma}/(3\mu)$ and the growth multiplier θ at the inner and outer radii of the annular plate are illustrated in Fig. 7(**b**). As can be seen from From Fig. 7(**a**), the maximum value of the area stretch occurs at the end of the growth stage with $t = 17$ s, and is calculated to be $A_{\text{max}}/A_0 = 4.8004$. After the unloading process, the final value of the area stretch is obtained to be $A_{\text{f}}/A_0 = 3.7209$. The maximum value of the growth parameter $\theta_{\mathfrak{g}}$ is 3.80, which is observed at the internal surface of the sheet.

(a) $t = 1$ s, $u_r^{out} = 6''$, $\theta_{\mathfrak{g}} = 1$

(b) $t = 5$ s, $u_r^{out} = 6''$

(c) $t = 9$ s, $u_r^{out} = 6''$

(d) $t = 13$ s, $u_r^{out} = 6''$

(e) $t = 17$ s, $u_r^{out} = 6''$

(f) $t = 18$ s, $F = 0$

Figure 6: Deformed shapes of the annular plate with the contour plots of the growth multiplier $\theta_{\mathfrak{g}}$ at different times
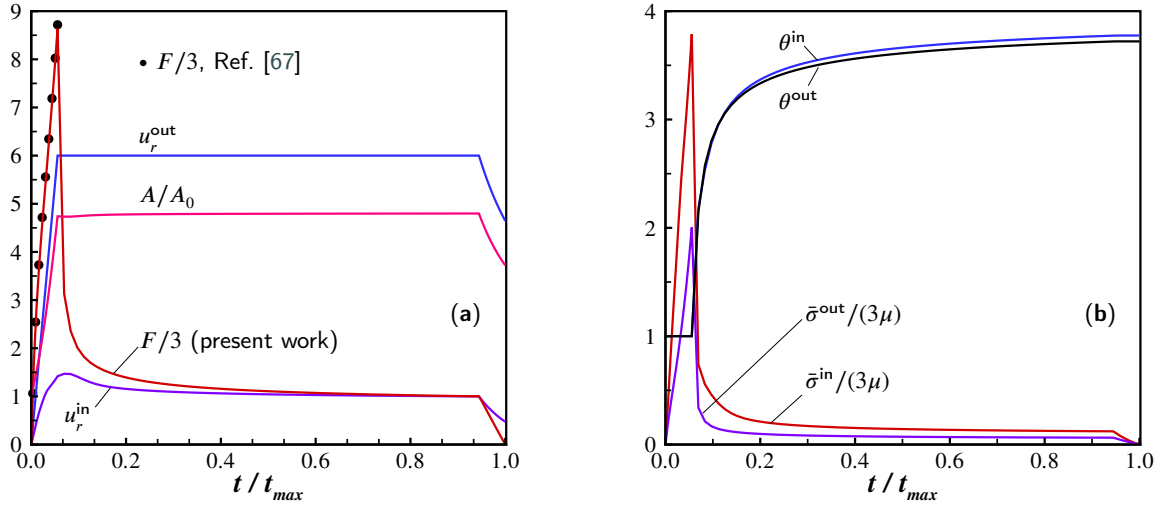
Figure 7: (**a**): Time history of radial displacements u_r^{in} and u_r^{out}, area stretch A/A_0, and the resultant force F, (**b**): time history of the non-dimensional von Mises stress $\bar{\sigma}/(3\mu)$ and the growth multiplier θ at the inner and outer radii of the annular plate

6.4. Growth of a tissue as a curved strip

In this example, the growth of soft tissue with an initial geometry as a curved strip is investigated. The strip can be a simple prototype of an S-shaped human spine. The geometry and loading are shown in Fig. 8(**a**). The referential average radius of curvature, width, and thickness of the strip are $R = \sqrt{2}$, $W = 0.04$, and $h = 0.04$ (m), respectively. Moreover, the projected length of the strip along the x_1-axis is $2L = 0.4$ (m). The left end of the centreline is immovable, while its right end can freely move in the x_1 direction. It is assumed that the strain energy density is the same as that given in the example 6.1. Following Ref. [39], the shear modulus and the growth parameters are considered to be $\mu = 0.0385$ MPa, $\theta_{\mathfrak{g}}^{\max} = 2.4$, $\gamma = 2$, $T = 1$ s, and $\theta_{\text{e}}^{\text{crit}} = 1.01$. Moreover, Poisson's ratio is considered to be $\nu = 0.48$. The force per unit length p is applied gradually from $p = 0$ to $p_{\max} = 30$ N/m in $t_{\mathfrak{l}} = 0.5$ s. The maximum load is then held constant for $t_{\mathfrak{g}} = 22$ s to observe the growth in the sheet. Finally, the unloading procedure from $p_{\max}$ to 0 is performed during $t_{\mathfrak{u}} = 1$ s. Accordingly, the maximum time of simulation is $t_{\max} = 23.5$ s.

Numerical simulations reveal that a mesh of 6×48 elements leads to convergent results. The deformed shapes of the strip for $t = 0.5, 5.5, 10.5, 15.5, 22.5$, and 23.5 (s) are displayed in Fig. 8(**a–f**). In particular, the deformed geometry at the end of pure elastic loading, corresponding to the time $t = 0.5$ s, is demonstrated in Fig. 8(**a**), where the growth multiplier is still $\theta_{\mathfrak{g}} = 1$ on the entire geometry. As can be seen from Figs. 8(**b–e**), by increasing the time in the interval $0.5 < t \leq 22.5$, the strip curvature increases gradually in the opposite direction of its initial one. Moreover, the growth multiplier $\theta_{\mathfrak{g}}$ follows an increasing trend. The final grown geometry is depicted in Fig. 8(**f**), where it is observed that the deformed strip is almost a straight line.
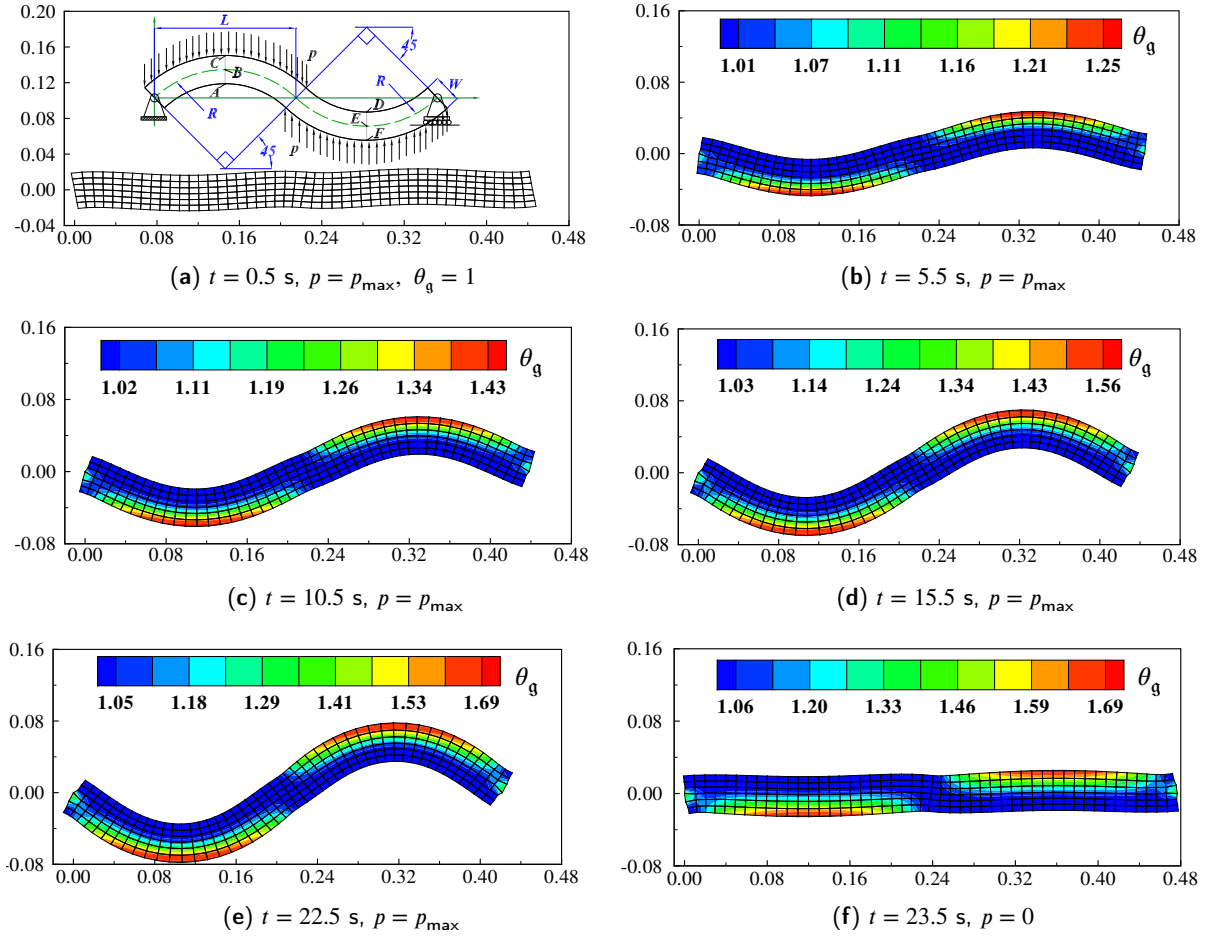
Figure 8: Deformed shapes of the curved strip with the contour plots of the growth multiplier $\theta_{\mathfrak{g}}$ at different times.

The curves corresponding to the strip centreline are illustrated in Fig. 9(**a**). It is noted that only the even load steps are plotted in the figure. Next, the material points $\{A, B, C, D, E, F\}$ as shown in Fig. 8(**a**) are considered. Due to the skew-symmetry of the geometry, the material points $\{D, E, F\}$ have the same properties of $\{A, B, C\}$, respectively. Time history of the growth parameter θ and the non-dimensional von Mises stress $\bar{\sigma}/(4\mu)$, for the material points $\{A, B, C\}$ are displayed in Fig. 9(**b**). Variation of the area stretch A/A_0 is also shown in the figure. From Fig. 9(**b**) it is observed that the maximum values of the von Mises stress $\bar{\sigma}$ occur at the material point C. However, the maximum value of the growth multiplier $\theta_{\mathfrak{g}}$ is observed at the material point A and attains its maximum value $\theta_{\max}^A = 1.75$. The maximum value of the area stretch takes place at the end of the growth stage with $t = 22.5$ s and is obtained to be $A_{\max}/A_0 = 1.16$. After the unloading stage, the final value of the area stretch is calculated to be $A_{\mathfrak{f}}/A_0 = 1.15$.
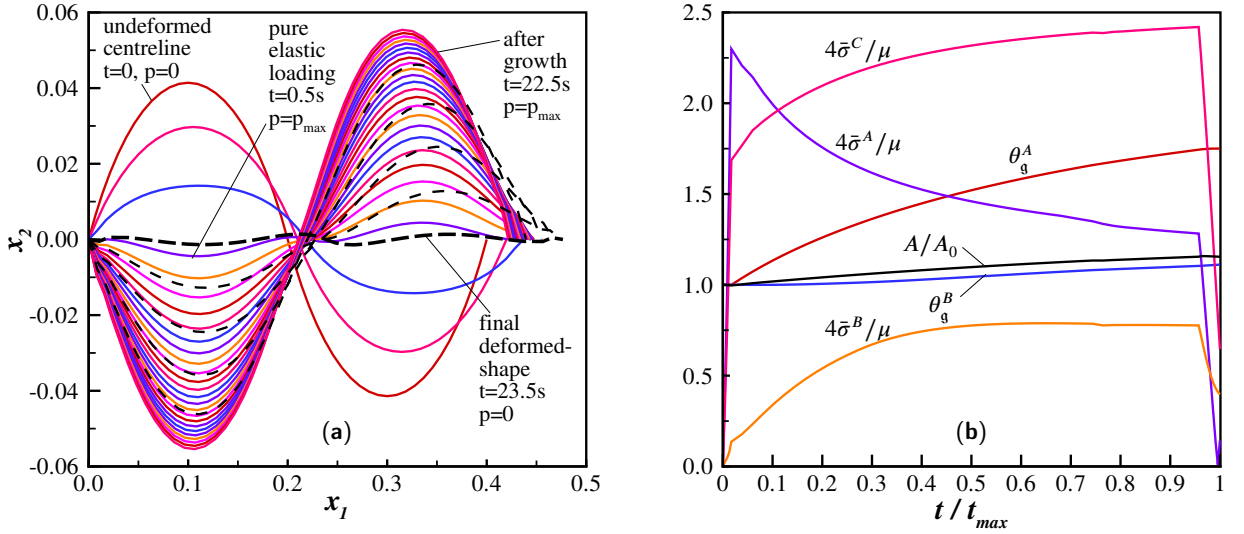
Figure 9: (**a**) Deformed shapes of the centreline at various time steps (even load steps are demonstrated, dashed lines correspond to the unloading stage), (**b**) time history of the area stretch A/A_0, and those of $\theta_{\mathfrak{g}}$ and $4\bar{\sigma}/\mu$ at some material points.

6.5. Growth of a thin-walled helix under self-weight

In this example, the growth mechanics of a helix under its weight is investigated. The cross-section of the helix is a circle of radius $a = 5$ mm and the thickness $h = 1$ mm. The average radius of the helix is $b = 25$ mm. The angle $\zeta^1 \in [0, 2\pi]$ describes the circumference of the cross-section. Moreover, the angle $\zeta^2 \in [0, \zeta^2_{\max}]$ is used to describe the centreline of the helix. In this work, $\zeta^2_{\max} = 6\pi$ is employed, which creates a helix with three complete loops. The equation of the referential centreline is given by

$$X_1^{\mathfrak{c}} = b \cos \zeta^2, \quad X_2^{\mathfrak{c}} = b \sin \zeta^2, \quad X_3^{\mathfrak{c}} = \frac{p}{2\pi} \zeta^2,$$

where p is the pitch of the helix, and is considered to be 12.5 mm. The undeformed geometry of the helix and its cross-section are displayed in Fig. 10(**a**). It is assumed that the strain energy density is the same as that given in the example 6.1. The material parameters are considered to be $\mu = 0.0385$ MPa, $\nu = 0.48$, $\theta_{\mathfrak{g}}^{\max} = 2.4$, $\gamma = 2$, $T = 0.1$ s, and $\theta_{\mathfrak{e}}^{\mathrm{crit}} = 1$. Moreover, the referential density is $\rho_0 = 20$ kg/m^3. The top cross-section of the helix, at $\zeta^2 = \zeta^2_{\max}$, is assumed to be fixed. In the first step, the weight of the helix is applied gradually in $t_{\mathfrak{l}} = 1$ s. The growth process under the maximum weight is then simulated in $t_{\mathfrak{g}} = 30$ s.

Numerical experiments show that a mesh of 10×90 elements is required to achieve convergent results. Now, the material points C_t and C_m, respectively, at $(\zeta^1 = \pi, \zeta^2 = 0)$ and $(\zeta^1 = \pi, \zeta^2 = \frac{1}{2}\zeta^2_{\max})$ are considered. The nondimensional displacement components u_i/b at the material points C_t and C_m against the nondimensional time
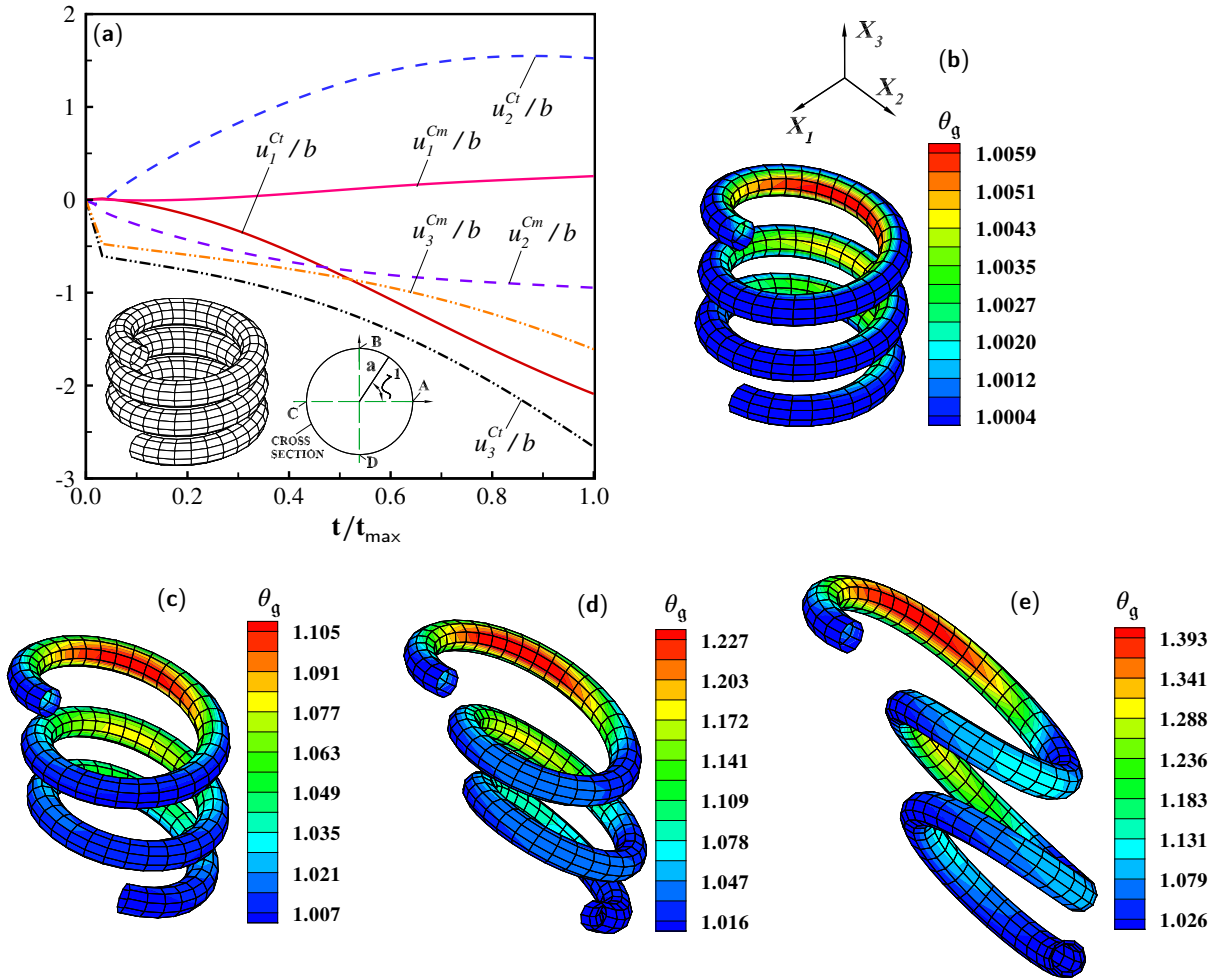
Figure 10: Growth of a helix under self-weight, (**a**): history of displacement at the points C_m and C_t, (**b**): deformed shape and contour plot of $\theta_{\mathfrak{g}}$ at the end of loading ($t = 1$ s), (**c**): grown stage at $t = 11$ s, (**d**): grown stage at $t = 21$ s, (**e**): grown stage at $t = 31$ s.

$t/t_{\max}$ are plotted in Fig. 10(**a**). Moreover, the deformed shapes of the helix at four stages, namely at $t \in \{1, 11, 21, 31\}$ (s) are illustrated in Fig. 10(**b–e**). The contour plots of the growth parameter $\theta_{\mathfrak{g}}$ are also displayed on the deformed shapes. The maximum value of $\theta_{\mathfrak{g}}$ is obtained to be 1.45.

6.6. Growth of a flower-like geometry

In this example, the growth of a geometry that is similar to a flower is investigated. If the flower is composed of N petals, by considering the $X_1 X_3$-plane as the plane of symmetry, the geometry of a single petal can be described by the meridian angle $\zeta^1 \in [\zeta_{\min}^1, \zeta_{\max}^1]$ and the polar angle $\zeta^2 \in [-\frac{\pi}{N}, \frac{\pi}{N}]$. It is noted that the meridian angle ζ^1 is measured with respect to the south pole. In this work, the values of $N = 8$, $\zeta_{\min}^1 = \frac{\pi}{36}$, and $\zeta_{\max}^1 = \frac{\pi}{3}$ are used in the simulations.

Moreover, we noted that the material points of a single petal may be described via the following equations:

$$X_1 = k_1 R \sin \zeta^1 \cos(f\zeta^2), \quad X_2 = k_1 R \sin \zeta^1 \sin(f\zeta^2), \quad X_3 = -R \cos \zeta^1,$$

where $f(\zeta^1) = \frac{\zeta^1_{\max} - k_2 \zeta^1}{\zeta^1_{\max} - k_2 \zeta^1_{\min}}$ is a scalar function. Moreover, $k_1 = 25$ and $k_2 = 0.98$ are two constants. From another point of view, the petal is part of the boundary surface of an ellipsoid whose equation is given by $(\frac{X_1}{k_1 R})^2 + (\frac{X_3}{k_1 R})^2 + (\frac{X_3}{R})^2 = 1$. The length of the semi-axis of the ellipsoid along X_3 and the initial thickness are, respectively, considered to be $R = 10$ and $h = 2$ (mm). The strain energy density is the same as that described in the example 6.1. Moreover, the material parameters are considered to be $\mu = 2$ MPa, $v = 0.48$, $\theta^{\max}_{\mathfrak{g}} = 2.4$, $\gamma = 2$, $T = 0.1$ s, and $\theta^{\mathrm{crit}}_{\mathrm{e}} = 1$. The petal is fixed at $\zeta^1 = \zeta^1_{\min}$, and its tip curve at $\zeta^1 = \zeta^1_{\max}$ is subjected to the force per unit length $q^1_{\max} = -2.5$ and $q^3_{\max} = 5$ (N/m) in the X_1 and X_3 directions, respectively. In the first step, the loads q^1 and q^3 are applied gradually to the petal from zero to their maximum values in $t_{\mathfrak{l}} = 1$ s. In the growth stage, the petal is subjected to the maximum values of q^1 and q^3 for $t_{\mathfrak{g}} = 30$ s. Finally, the loads are gradually deceased from their maximum values to zero in $t_{\mathfrak{u}} = 1$ s. Accordingly, the maximum time of simulation is $t_{\max} = 32$ s.

Due to symmetry, only one-half of a petal is discretized by the shell elements. A mesh of 4×24 elements leads to convergent results. Next, the material points A and B along the centreline of the petal are considered. The point A is located at the tip of the centreline, but the meridian angle of the point B is given by $\zeta^1_B = \frac{1}{2}(\zeta^1_{\min} + \zeta^1_{\max})$. The nondimensional displacement components u_1/R and u_3/R at the material points A and B versus the nondimensional time $t/t_{\max}$ are depicted in Fig. 11(**a**). It is noted that the maximum values of lateral deflection at the point A at the end of the growth stage and after unloading are 149.46 and 84.06 (mm), respectively. Finally, the deformed shapes of the helix at four stages, namely at $t \in \{1, 16, 31, 32\}$ (s) are demonstrated in Fig. 11(**b–e**). The contour plots of the growth parameter $\theta_{\mathfrak{g}}$ are also displayed on the deformed shapes. Moreover, the maximum calculated value of $\theta_{\mathfrak{g}}$ is 1.16.

7. Summary

The finite growth of shell-like soft tissues subject to mechanical loading was investigated in this work. The essential kinematic quantities and the constitutive equations describing the combined deformation and growth of thin living bodies were presented. In particular, the expression for the tangent modulus contains additional terms, besides the traditional one, due to the growth effects. Moreover, a finite element formulation, in material framework, for the numerical solution of the nonlinear governing equations was developed. Several benchmark examples were provided that reveal the applicability of the proposed formulation. It was shown that the present formulation is successful in predicting the simultaneous deformation and growth of thin shell-like tissues subject to mechanical loads under a wide variety of boundary conditions. Therefore, it can be used for design and analysis purposes in bionic and
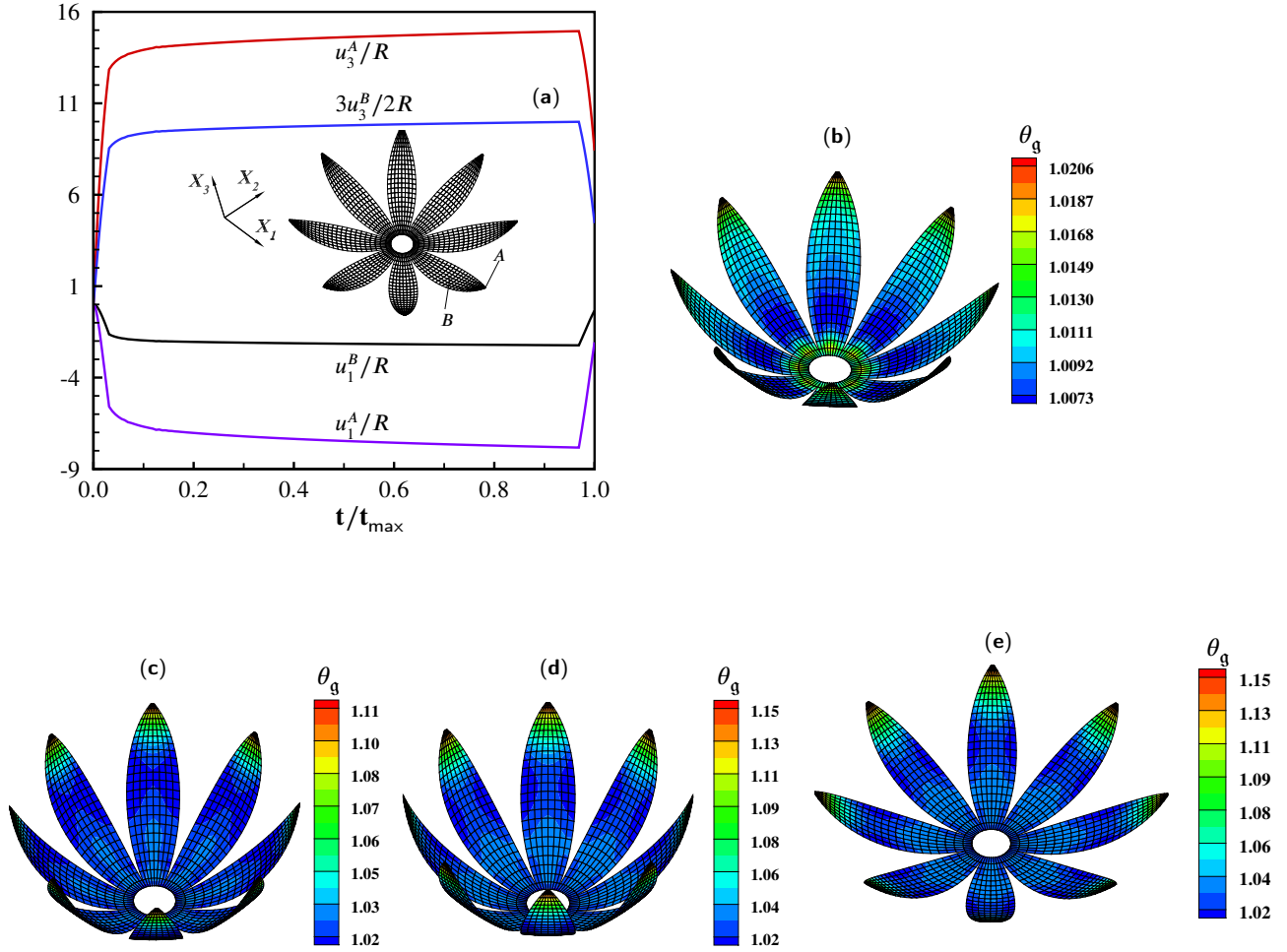
Figure 11: Growth of a flower-type geometry, (**a**): displacement components vs time at the points A and B, (**c**): deformed shape and contour plot of $\theta_{\mathfrak{g}}$ at the end of loading stage ($t = 1$ s), (**d**): growth stage at $t = 16$ s, (**d**): end of growth stage ($t = 31$ s), (**e**): end of unloading stage ($t = 32$ s).

tissue engineering. An extension of the present work to account for temperature effects will be provided in the next contributions.

Appendix

The fourth-order tensor $\mathcal{C}$ is given by (see also, Refs. [39, 43, 44])

$$\mathcal{C} = 2\frac{\mathrm{d}\mathbf{S}}{\mathrm{d}\mathbf{C}} = 2\left[\frac{\partial\mathbf{S}}{\partial\mathbf{C}}\bigg|_{\mathbf{F}_{\mathfrak{g}}} + \left(\frac{\partial\mathbf{S}}{\partial\mathbf{F}_{\mathfrak{g}}} : \frac{\partial\mathbf{F}_{\mathfrak{g}}}{\partial\mathbf{C}}\right)\bigg|_{\mathbf{F}}\right] = 2\left[\frac{\partial\mathbf{S}}{\partial\mathbf{C}}\bigg|_{\mathbf{F}_{\mathfrak{g}}} + \left(\frac{\partial\mathbf{S}}{\partial\mathbf{F}_{\mathfrak{g}}} : \frac{\partial\mathbf{F}_{\mathfrak{g}}}{\partial\theta_{\mathfrak{g}}} \otimes \frac{\partial\theta_{\mathfrak{g}}}{\partial\mathbf{C}}\right)\bigg|_{\mathbf{F}}\right]. \tag{A-1}$$

In the sequel, the derivative terms that appeared in Eq. (A-1) are calculated. To do so, from Eqs. $(10)_1$ and $(23)_1$, the first term in the brackets may be written as

$$\left.\frac{\partial \mathbf{S}}{\partial \mathbf{C}}\right|_{\mathbf{F}_g} = \left.\frac{\partial}{\partial \mathbf{C}}(\mathbf{F}_g^{-1}\mathbf{S}_e\mathbf{F}_g^{-\top})\right|_{\mathbf{F}_g} = \mathbf{F}_g^{-1}\left(\frac{\partial \mathbf{S}_e}{\partial \mathbf{C}_e}:\frac{\partial \mathbf{C}_e}{\partial \mathbf{C}}\right)\mathbf{F}_g^{-\top} = \frac{1}{2}\boldsymbol{\mathcal{F}}_1:\boldsymbol{\mathcal{C}}_e:\boldsymbol{\mathcal{F}}_2. \tag{A-2}$$

where the fourth-order tensors $\boldsymbol{\mathcal{C}}_e$ and $\boldsymbol{\mathcal{F}}_{\mathcal{I}}$ ($\mathcal{I} = 1, 2$) are defined as follows:

$$\boldsymbol{\mathcal{C}}_e = 2\frac{\partial \mathbf{S}_e}{\partial \mathbf{C}_e}, \quad \boldsymbol{\mathcal{F}}_1 = \mathbf{F}_g^{-1} \boxtimes \mathbf{F}_g^{-\top}, \quad \boldsymbol{\mathcal{F}}_2 = \mathbf{F}_g^{-\top} \odot \mathbf{F}_g^{-1}. \tag{A-3}$$

Similarly, Eqs. $(10)_2$ and $(23)_1$ leads to the following expression for the term $\left.\frac{\partial \mathbf{S}}{\partial \mathbf{F}_g}\right|_{\mathbf{F}}$:

$$\begin{aligned}
\left.\frac{\partial \mathbf{S}}{\partial \mathbf{F}_g}\right|_{\mathbf{F}} &= \left.\frac{\partial}{\partial \mathbf{F}_g}(\mathbf{F}_g^{-1}\mathbf{S}_e\mathbf{F}_g^{-\top})\right|_{\mathbf{F}} \\
&= \left[\frac{\partial \mathbf{F}_g^{-1}}{\partial \mathbf{F}_g}\mathbf{S}_e\mathbf{F}_g^{-\top} + \mathbf{F}_g^{-1}\mathbf{S}_e\frac{\partial \mathbf{F}_g^{-\top}}{\partial \mathbf{F}_g} + \mathbf{F}_g^{-1}\left(\frac{\partial \mathbf{S}_e}{\partial \mathbf{C}_e}:\frac{\partial \mathbf{C}_e}{\partial \mathbf{F}_g}\right)\mathbf{F}_g^{-\top}\right]_{\mathbf{F}} \\
&= -\frac{1}{2}\left(2\boldsymbol{\mathcal{F}}_3 + \boldsymbol{\mathcal{F}}_1:\boldsymbol{\mathcal{C}}_e:\boldsymbol{\mathcal{F}}_4\right),
\end{aligned} \tag{A-4}$$

where the fourth-order tensors $\boldsymbol{\mathcal{F}}_3$ and $\boldsymbol{\mathcal{F}}_4$ are given by

$$\boldsymbol{\mathcal{F}}_3 = \mathbf{F}_g^{-1} \odot \mathbf{S} + \mathbf{S} \boxtimes \mathbf{F}_g^{-\top}, \quad \boldsymbol{\mathcal{F}}_4 = \mathbf{F}_g^{-\top} \boxtimes \mathbf{C}_e + \mathbf{C}_e\bar{\boxtimes}\mathbf{F}_g^{-1}. \tag{A-5}$$

To calculate $\frac{\partial \theta_g}{\partial \mathbf{C}}$, in the first step, straightforward calculations lead to the following expression for $\frac{\partial \theta}{\partial \mathbf{C}}$:

$$\frac{\partial \theta}{\partial \mathbf{C}} = \frac{1}{2\theta}\left[\theta^2\mathbf{I} - J^2\mathbf{C}^{-1}(\mathbb{D} \otimes \mathbb{D})\right]\mathbf{C}^{-1}, \tag{A-6}$$

where use has been made of $\frac{\partial \mathbf{C}^{-1}}{\partial \mathbf{C}} = -\frac{1}{2}(\mathbf{C}^{-1} \boxtimes \mathbf{C}^{-1} + \mathbf{C}^{-1} \odot \mathbf{C}^{-1})$ and $\frac{\partial J^2}{\partial \mathbf{C}} = J^2\mathbf{C}^{-1}$ (e.g., Ref. [65]). Next, differentiating the scalar function β, defined in Eqs. (15) and (16), with respect to θ and $\mathbf{C}$ furnishes

$$\frac{\partial \beta}{\partial \theta} = \frac{\Phi_1}{\theta_g}, \quad \frac{\partial \beta}{\partial \mathbf{C}} = \frac{\partial \beta}{\partial \theta_g}\frac{\partial \theta_g}{\partial \mathbf{C}} + \frac{\partial \beta}{\partial \theta}\frac{\partial \theta}{\partial \mathbf{C}}. \tag{A-7}$$

By discarding the superscript "$n + 1$" in Eq. (47), differentiating with respect to $\mathbf{C}$, using Eqs. $(48)_2$ and (A-7), and solving for $\frac{\partial \theta_g}{\partial \mathbf{C}}$ one obtains

$$\frac{\partial \theta_g}{\partial \mathbf{C}} = \frac{\Phi_1\Delta t}{K\theta_g}\frac{\partial \theta}{\partial \mathbf{C}} = \frac{\Phi_1\Delta t}{2K\theta\theta_g}\left[\theta^2\mathbf{I} - J^2\mathbf{C}^{-1}(\mathbb{D} \otimes \mathbb{D})\right]\mathbf{C}^{-1}, \tag{A-8}$$

where use has been made of Eq. (A-6) in the last expression. Now, by back substituting Eqs. $(12)_4$, (A-2), (A-4), and (A-8) into (A-1), the fourth-order elasticity tensor C is obtained.

References

[1] L.A. Taber, Biomechanics of growth, remodeling, and morphogenesis, Applied Mechanics Reviews 48 (1995) 487–545.

[2] C. Vignes, P. Papadopoulos, Material growth in thermoelastic continua: Theory, algorithmics, and simulation, Computer Methods in Applied Mechanics and Engineering 199 (2010) 979–996.

[3] D. Ambrosi, F. Guana, Stress-modulated growth, Mathematics and mechanics of solids 12 (2007) 319–342.

[4] H.A. Benhardt, E.M. Cosgriff-Hernandez, The role of mechanical loading in ligament tissue engineering. Tissue Engineering: Part B 15 (2009) 467.

[5] Y.U. Lee, D. Hayman, E.A. Sprague, H.C. Han, Effects of axial stretch on cell proliferation and intimal thickness in arteries in organ culture, Cellular and Molecular Bioengineering 3 (2010) 286–295.

[6] B.D. Riehl, J-H. Park, I.K. Kwon, J.Y. Lim, Mechanical stretching for tissue engineering: two-Dimensional and three-dimensional constructs, Tissue Engineering: Part B 18 (2012) 288–300.

[7] Y. Liu, H. Zhang, Y. Zheng, S. Zhang, B. Chen, A nonlinear finite element model for the stress analysis of soft solids with a growing mass, International Journal of Solids and Structures 51 (2014) 2964–2978.

[8] A. Goriely, The mathematics and mechanics of biological growth, Springer, NY, 2017.

[9] C. Liu, Y. Du, C. Lü, W. Chen, Growth and patterns of residually stressed core–shell soft sphere, International Journal of Non-Linear Mechanics 127 (2020) 103594.

[10] E.K. Rodriguez, A. Hoger, A.D. McCulloch, Stress-dependent finite growth in soft elastic tissues, Journal of Biomechanics 27 (1994) 455-467.

[11] M. Epstein, G.A. Maugin, Thermomechanics of volumetric growth in uniform bodies, International Journal of Plasticity 16 (2000) 951–978.

[12] V.A. Lubarda, A. Hoger, On the mechanics of solids with a growing mass, International Journal of Solids and Structures 39 (2002) 4627–4664.

[13] G. Himpel, E. Kuhl, A. Menzel, P. Steinmann, Computational modelling of isotropic multiplicative growth, Computer Modeling in Engineering & Sciences 8 (2005) 119–134.

[14] A. Menzel, A fibre reorientation model for orthotropic multiplicative growth, Biomechanics and Modeling in Mechanobiology 6 (2007) 303–320.

[15] G.W. Jones, S.J. Chapman, Modeling growth in biological materials, SIAM Review 54 (2012) 52–118.

[16] A. Grillo, S. Federico, G. Wittum, Growth, mass transfer, and remodeling in fiber-reinforced, multi-constituent materials, International Journal of Non-Linear Mechanics 47 (2012) 388–401.

[17] A. Yavari, A geometric theory of growth mechanics, Journal of Nonlinear Science 20 (2010) 781–830.

[18] M. Javadi, M. Asghari, S. Sohrabpour, Material growth and remodeling formulation based on the finite couple stress theory, International Journal of Non-Linear Mechanics 121 (2020) 103413.

[19] M. Javadi, M. Epstein, M. Asghari, Thermomechanics of material growth and remodeling in uniform bodies based on the micromorphic theory, Journal of the Mechanics and Physics of Solids 138 (2020) 103904.

[20] P. Ciarletta, M. Ben Amar, Growth instabilities and folding in tubular organs: A variational method in non-linear elasticity, International Journal of Non-Linear Mechanics 47 (2012) 248–257.

[21] M. Soleimani, N. Muthyala, M. Marino, P. Wriggers, A novel stress-induced anisotropic growth model driven by nutrient diffusion: theory, FEM implementation and applications in bio-mechanical problems, Journal of the Mechanics and Physics of Solids 144 (2020) 104097.

[22] Y. Liu, Z. Zhang, G. Devillanova, Z. Cai, Surface instabilities in graded tubular tissues induced by volumetric growth, International Journal of Non-Linear Mechanics 127 (2020) 103612.

[23] A. Javili, B. Dortdivanlioglu, E. Kuhl, C. Linder, Computational aspects of growth-induced instabilities through eigenvalue analysis, Computational Mechanics 56 (2015) 405–420.

[24] B. Dortdivanlioglu, A. Javili, C. Linder, Computational aspects of morphological instabilities using isogeometric analysis, Computer Methods in Applied Mechanics and Engineering 316 (2017) 261-279.

[25] S. Wang, N. Demirci, M. A. Holland, Numerical investigation of biomechanically coupled growth in cortical folding, Biomechanics and Modeling in Mechanobiology 20 (2021) 555–567.

[26] D. Ambrosi, F. Mollica, On the mechanics of a growing tumor, International Journal of Engineering Science 40 (2002) 1297–1316.

[27] H. Liang, L. Mahadevan, Growth, geometry, and mechanics of a blooming lily, Proceedings of the National Academy of Sciences 108 (2011) 5516–5521.

[28] M.A. Holland, T. Kosmata, A. Goriely, E. Kuhl, On the mechanics of thin films and growing surfaces, Mathematics and Mechanics of Solids 18 (2013) 561–575.

[29] P. Ciarletta, D. Ambrosi, G. Maugin, L. Preziosi, Mechano-transduction in tumour growth modelling, The European Physical Journal E 36 (2013) 1–9.

[30] X. Chen, H. H. Dai, Stress-free configurations induced by a family of locally incompatible growth functions. Journal of the Mechanics and Physics of Solids 137 (2020) 103834.

[31] C. Kadapa, Z. Li, M. Hossain, J. Wang, On the advantages of mixed formulation and higher-order elements for computational morphoelasticity, Journal of the Mechanics and Physics of Solids 148 (2021) 104289.

[32] G.W. Jones, L. Mahadevan, Optimal control of plates using incompatible strains, Nonlinearity 28 (2015) 3153–3174.

[33] J. Wang, Q. Wang, H-H. Dai, P. Dua, D. Chen, Shape-programming of hyperelastic plates through differential growth: an analytical approach, Soft Matter 15 (2019) 2391–2399.

[34] Z. Li, Q. Wang, P. Du, C. Kadapa, M. Hossain, J. Wang, Analytical study on growth-induced axisymmetric deformations and shape-control of circular hyperelastic plates, International Journal of Engineering Science 170 (2022) 103594.

[35] J. Wang, Z. Li, Z. Jin, A theoretical scheme for shape-programming of thin hyperelastic plates through differential growth, Mathematics and Mechanics of Solids (2022) https://doi.org/10.1177/10812865221089694.

[36] Z. Li, J. Wang, M. Hossain, C. Kadapa, A theoretical scheme for shape-programming of thin hyperelastic shells through differential growth, International Journal of Solids and Structures, 265-266:112128, 2023.

[37] Z. Li, C. Kadapa, M. Hossain, J. Wang, A numerical framework for the simulation of coupled electromechanical growth, Computer Methods in Applied Mechanics and Engineering, 414:116128, 2023.

[38] E. Kuhl, R. Maas, G. Himpel, A. Menzel, Computational modeling of arterial wall growth, Biomechanics and Modeling in Mechanobiology 6 (2007) 321–331.

[39] A.B. Tepole, C.J. Ploch, J. Wong, A.K. Gosain, E. Kuhl, Growing skin: a computational model for skin expansion in reconstructive surgery, Journal of the Mechanics and Physics of Solids 59 (2011) 2177–2190.

[40] M.K. Rausch, A. Dam, S. Göktepe, O.J. Abilez, E. Kuhl, Computational modeling of growth: systemic and pulmonary hypertension in the heart, Biomechanics and Modeling in Mechanobiology 10 (2011) 799–811.

[41] A. Buganza Tepole A.K. Gosain, E. Kuhl, Stretching skin: The physiological limit and beyond, International Journal of Non-Linear Mechanics 47 (2012) 938–949.

[42] M.K. Rausch, F.A. Tibayan, D.C. Miller, E. Kuhl, Evidence of adaptive mitral leaflet growth, Journal of the Mechanical Behavior of Biomedical Materials 15 (2012) 208–217.

[43] A.M. Zöllner, A.B. Tepole, E. Kuhl, On the biomechanics and mechanobiology of growing skin, Journal of Theoretical Biology 297 (2012) 166–175.

[44] A.M. Zöllner, A.B. Tepole, A.K. Gosain, E. Kuhl, Growing skin: tissue expansion in pediatric forehead reconstruction, Biomechanics and Modeling in Mechanobiology 11 (2012) 855–867.

[45] A.B. Tepole, M. Gart, A.K. Gosain, E. Kuhl, Characterization of living skin using multi-view stereo and isogeometric analysis, Acta Biomaterialia 10 (2014) 4822–4831.

[46] S. Budday, P. Steinmann, E. Kuhl, The role of mechanics during brain development, Journal of the Mechanics and Physics of Solids 72 (2014) 75–92.

[47] T. Lee, M.A. Holland, J. Weickenmeier, A.K. Gosain, A.B. Tepole, The geometry of incompatibility in growing soft tissues: Theory and numerical characterization, Journal of the Mechanics and Physics of Solids 146 (2021) 104177.

[48] J. Dervaux, P. Ciarletta, M. Ben Amar, Morphogenesis of thin hyperelastic plates: a constitutive theory of biological growth in the Föppl–von Kármán limit, Journal of the Mechanics and Physics of Solids 57(2009) 458–471.

[49] J. Wang, D. Steigmann, F.-F. Wang, H.-H. Dai, On a consistent finite-strain plate theory of growth, Journal of the Mechanics and Physics of Solids 111 (2018) 184–214.

[50] J. Wang, Q. Wang, H-H. Dai, Stress-free bending of a neo-Hookean plate induced by growth: Exact solution and experiments, International Journal of Non-Linear Mechanics 106 (2018) 280–287.

[51] P. Du, H.-H. Dai, J. Wang, Q. Wang, Analytical study on growth-induced bending deformations of multi-layered hyperelastic plates, International Journal of Non-Linear Mechanics 119 (2020) 103370.

[52] M.K. Rausch, E. Kuhl, On the mechanics of growing thin biological membranes, Journal of the Mechanics and Physics of Solids 63 (2014) 128–140.

[53] Abaqus 6.12, Analysis User's Manual. SIMULIA. Dassault Systémes, 2012.

[54] Y. Zheng, J. Wang, H. Ye, Y. Liu, H. Zhang, A solid-shell based finite element model for thin-walled soft structures with a growing mass, International Journal of Solids and Structures (2018) 163 (2019) 87–101.

[55] J.A. Cottrell, T.J.R. Hughes, Y. Bazilevs, Isogeometric Analysis: Toward Integration of CAD and FEA, Wiley, NY, 2009.

[56] A.B. Tepole, H. Kabaria, K.U. Bletzinger, E. Kuhl, Isogeometric Kirchhoff–Love shell formulations for biological membranes, Computer methods in applied mechanics and engineering 293 (2015) 328–347.

[57] S. Sadik, A. Angoshtari, A. Goriely, A. Yavari, A geometric theory of nonlinear morphoelastic shells, Journal of Nonlinear Science 26 (2016) 929–978.

[58] C. Sansour, Large strain deformations of elastic shells, constitutive modelling and finite element analysis, Computer Methods in Applied Mechanics and Engineering 161 (1998) 1–18.

[59] C. Sansour, F.G. Kollmann, Families of 4-node and 9-node finite elements for a finite deformation shell theory, an assessment of hybrid stress, hybrid strain and enhanced strain elements, Computational Mechanics 24 (2000) 435–447.

[60] J.C. Simo, F. Armero, Geometrically non-linear enhanced strain mixed methods and the method of incompatible modes, International Journal for Numerical Methods in Engineering 33 (1992) 1413–1449.

[61] J.C. Simo, F. Armero, R.L. Taylor, Improved versions of assumed enhanced strain tri-linear elements for 3D finite deformation problems, Comput. Methods Appl. Mech. Eng. 110 (1993) 359–386.

[62] S. Klinkel, W. Wagner, A geometrical non-linear brick element based on the EAS-method, International Journal for Numerical Methods in Engineering 40 (1997) 4529–4545.

[63] S. Glaser, F. Armero, On the formulation of enhanced strain finite elements in finite deformations, Eng. Comput. 14 (1997) 759–791.

[64] M. Itskov, Tensor Algebra and Tensor Analysis for Engineers, Springer, 2019.

[65] G.A. Holzapfel, Nonlinear Solid Mechanics, A Continuum Approach for Engineering, Wiley, NY, 2000.

[66] N. Büchter, E. Ramm, D. Roehl, 3-Dimensional extension of nonlinear shell formulation based no the enhanced assumed strain concept, International Journal for Numerical Methods in Engineering 37 (1994) 2551–2568.

[67] E.A.D. de Souza Neto, D. Peric, D.R.J. Owen, Finite elasticity in spatial description: linearization aspects with 3-D membrane applications, International Journal for Numerical Methods in Engineering 38 (1995) 3365–3381.